Lethaia
AN INTERNATIONAL JOURNAL OF PALAEONTOLOGY AND STRATIGRAPHY

Radiolitid rudists: an underestimated archive for Cretaceous climate reconstruction?

KATHARINA E. SCHMITT, STEFAN HUCK, MALTE KRUMMACKER, NIELS J. DE WINTER, ALEXIS GODET, PHILIP CLAEYS AND ULRICH HEIMHOFER

LETHAIA

Rudist shells are important archives for palaeoenvironmental reconstructions in the greenhouse world of the Cretaceous. Radiolitids, a family of rudists became very abundant dwellers of the shallow marine carbonate platforms during the Cretaceous. Still, due to the complex structure of their low-Mg calcite outer shell layer, radiolitids are often deemed unsuitable for palaeoenvironmental reconstructions. The aim of this study is to present a combination of petrographic (transmitted light microscopy and cathodoluminescence microscopy) and elemental analyses (high-resolution μXRF and stable isotope) to investigate radiolitid shells for diagenetic alteration and to make them accessible as an archive for environmental conditions during the mid-Cretaceous. Four *Eoradiolitites* shells were analysed in detail: two right valves (RV), a left valve (LV) with an articulated RV and an isolated LV. Three shell structure types have been identified, including a non-compact, compact and cellulоprismatic types. The compact structure type was identified in the LVs while the other two types were observed exclusively in the RVs. Radiolitid shell material composed of the non-compact and the compact structure types can be used as palaeoenvironmental archives as it preserved seasonal signals in both, shell growth structure and isotopic records, while cellulоprismatic shell structures are less suitable for reconstructions due to diagenetic alteration. The alternation of dark and light lamellae in both valves, RV and LV, provide information on the intertidal living habitat of the shell-producing organism and its life span. □ *Cretaceous; radiolitid rudists; petrographic and rlemental analyses; right and left valves; palaeoenvironmental reconstruction*

Katharina E. Schmitt ✉ [Katharina.Schmitt@uni-mainz.de], *Institute of Geosciences, University of Mainz, Johann-Joachim-Becher-Weg 21, 55128 Mainz, Germany;* Ulrich Heimhofer [heimhofer@geowi.uni-hannover.de], *Leibniz Universität Hannover, Institut für Geologie, Callinstraße 30, D-30167 Hannover, Germany;* Stefan Huck [Stefan.Huck@spar-bau.de], *Spar- und Bauverein eG, Arndtstraße 5, 30167 Hannover;* Malte Krummacker [maltekrummacker@googlemail.com], *Schnack Ingenieurgesellschaft mbH & Co. KG, Güntherstraße 47, 30519 Hannover;* Niels J. de Winter [Niels.De.Winter@vub.be], *Vrije Universiteit Brussel, Analytical, Environmental and Geochemistry (AMGC) Group, Pleinlaan 2, 1050 Brussels, Belgium*; Philippe Claeys [phclaeys@vub.be], *Vrije Universiteit Brussel, Analytical, Environmental and Geochemistry (AMGC) Group, Pleinlaan 2, 1050 Brussels, Belgium;* Alexis Godet [Alexis.Godet@utsa.edu], *Department of Earth and Planetary Sciences, University of Texas at San Antonio, 1 UTSA Circle, San Antonio, TX 78249, USA;* *manuscript received on 04/02/2022; manuscript accepted on 15/07/2022; manuscript published on 23/11/2022 in* Lethaia 55(4).

The climate of the mid-Cretaceous was characterized by prolonged greenhouse conditions, which were only interrupted by a few short-lived but prominent cooling events (Skelton *et al.* 2003; Steuber *et al.* 2005; Bornemann *et al.* 2008; Mutterlose *et al.* 2009). Cretaceous ocean water temperatures are predominantly reconstructed using $\delta^{18}O$ data derived from belemnites (e.g. Bodin *et al.* 2015) and planktonic foraminifera (e.g. Bottini *et al.* 2015), and TEX_{86} (e.g. O'Brien *et al.* 2017). As the seasonal organisms were floating or migrating through the water column, their isotope records contain a mix of temperatures from various habitats (e.g. Eggins *et al.* 2003). In contrast, biogenic calcite shells produced by shallow marine and sessile molluscs with a multi-year lifespan can provide information on seasonal variability of sea-surface temperatures.

In the Cretaceous, sessile rudist bivalves (superfamily Hippuritacea) dominated shallow marine, low latitude carbonate platform settings and have been used in numerous studies for palaeoenvironmental reconstructions (Ross & Skelton 1993; Scott *et al.* 1995; Skelton & Gili 2012; Steuber & Schlüter 2012; de Winter *et al.* 2017a, Huck & Heimhofer 2021). Following their first appearance in the Oxfordian (Late Jurassic) (Skelton 1978), they evolved to become the most important carbonate-producing biota (Steuber & Veizer 2002) in Cretaceous low-latitude shelf seas until they went

https://doi.org/10.18261/let.55.4.4

extinct at the Cretaceous/Paleogene boundary (Skelton *et al.* 2003; Steuber & Schlüter 2012).

Although various forms had evolved over time, all species can be assigned to one of three morphotypes, recumbents, clingers or elevators, which were identified in previous ecological morphology studies (Schumann & Steuber 1997; Skelton & Gili 1991). All species built shells following a similar basic shell design: an outer layer composed of fibrous prismatic low-Mg calcite and at least one (sometimes two) inner aragonitic layer(s) (Kennedy & Taylor 1968; Skelton 1974; Sanders 1999; Pons & Vicens 2008). The aragonitic parts are usually replaced by diagenetic low-Mg calcite during fossilization, but the outer low-Mg calcite layer provides material with a high potential to act as an archive for seawater chemistry, as it is resistant to diagenesis (Al-Aasm & Veizer 1986a, b). For instance, prior studies have shown that the outer low-Mg calcite layer of Cretaceous rudist shells is a valuable archive for the strontium isotope composition of ocean waters (Steuber *et al.* 2005; Frijia & Parente 2008; Frijia *et al.* 2015; Huck & Heimhofer 2015). Additionally, it is suitable as palaeoenvironmental archive as the secreting processes of the shells were affected by palaeoclimatic (seasonal temperature variations), palaeochemical (salinity changes) and palaeobiological (growth rate and carbonate production) parameters (e.g. Steuber 1996; Regidor-Higuera *et al.* 2007; de Winter *et al.* 2017a; Huck & Heimhofer 2021).

Rudists have proven to be very suitable for climate reconstruction in the Cretaceous (Steuber *et al.* 2005). However, as different families with diverse shell structures and shapes evolved and became dominant during the course of the Cretaceous, there are episodes in which the climate record is incomplete as suitable material is missing. For example, Radiolitidae, a family typically overlooked as a palaeoclimatic archive due to its shell structure, spread in the Late Aptian-Albian and became the most abundant family among the rudists (Masse & Maresca 1997; Fenerci-Masse *et al.* 2006; Skelton & Gili 2012; Masse *et al.* 2007; Steuber & Löser 2000). Their taxonomy was discussed and defined in various previous studies (Pons & Vicens 2008; Cestari 1992; Schumann 1995; Skelton 1978). In general, their right, attached valve (RV) is described as conical to cylindro-conical, while the left, free valve (LV) is reduced to a cap-like form with a compact internal structure (Pons & Vicens 2008). The most significant feature of radiolitid shells is the distinct structure in the outer layer of their RV, which appears to be more (Regidor-Higuera *et al.* 2007; Tibljaš *et al.* 2004) or less pronounced (Steuber 1994; Pejović 2002), depending on the species. This portion is often described as honeycomb (Woo *et al.* 1993; Steuber 1999), boxwork (Hamama 2010), cellular (Masse & Maresca 1997; Masse *et al.* 2007) or celluloprismatic structure (Pons & Vicens 2008). It is formed by two kinds of laminae (or plates): the funnel plates and the radial plates (muri or walls). The latter are arranged orthogonal to the funnel plates (Masse *et al.* 2007) creating an intraskeletal pore space (Fig. 1), which was probably originally filled with organic material

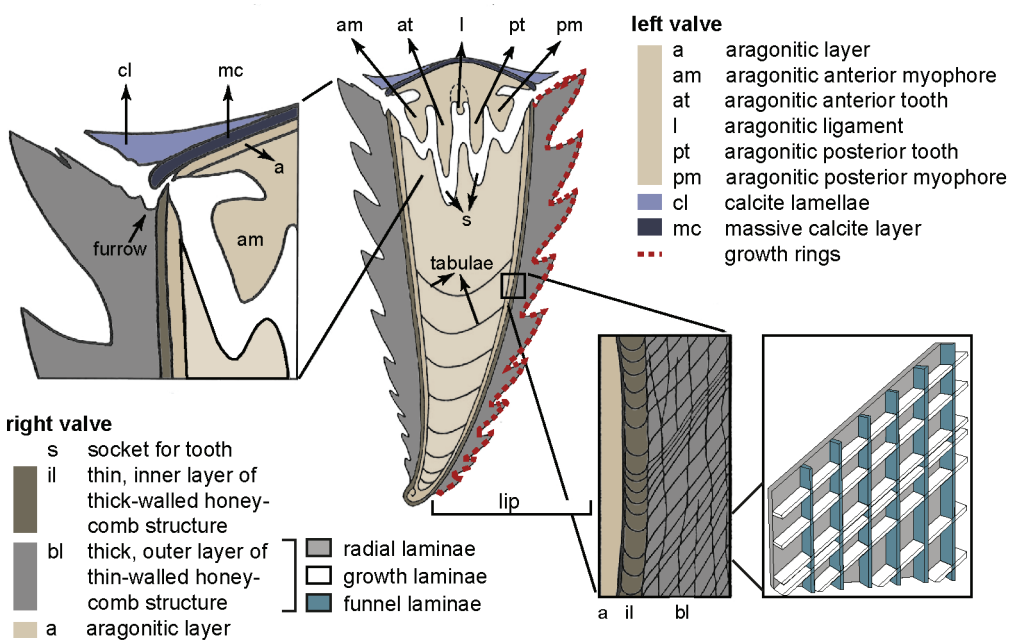

Fig. 1. Schematic structure of a radiolitid shell showing the cone shaped lower (right) valve with detailed view of the boxwork structure and the cap like upper (left) valve (modified after Sanders 1999; Pons & Vicens 2008).

(Regidor-Higuera *et al.* 2007). This material decomposed after the organism's death and the intraskeletal space was filled post-mortem (Tibljaš *et al.* 2004; Mansour 2004). For a more detailed description of the radiolitid shell structure, please refer to Regidor-Higuera *et al.* (2007).

Only few studies deal with the elemental and isotopic composition of radiolitid shells (Steuber 1999; Regidor-Higuera *et al.* 2007; Tibljaš *et al.* 2004). All authors agree that if the radiolitid contained a pronounced cellulosprismatic structure, this porous outer shell layer contains now diagenetic calcite, as fluids circulated through the pores causing its precipitation (Al-Aasm & Veizer 1986; Steuber 1999; Regidor-Higuera *et al. 2007*), making these species not suitable for palaeoenvironmental reconstructions. Nevertheless, the outer shell layer of radiolitids contains micro- and megarhythms, which are interpreted to be caused by seasonal, tidal or biological cycles (Sanders 1999; Pons & Vicens 2008). Megarhythms (assigned to annual cyclicity) are defined as major variations in shell ornamentation, visible in petrographic thin sections as a change in the microstructure or in variations in the stable oxygen isotope signal. Finer scale growth lamellae are designated as microrhythms expressed as a change in colour (light and dark) (Regidor-Higuera *et al.* 2007).

The aims of this study are twofold: (1), the identification of diagenetically altered shell parts by combining high-resolution geochemical analyses (isotope ratio mass spectrometry and micro-X-ray fluorescence) and classical sclerochronology (macro- and microstructures); and (2), testing the suitability of radiolitid shells as palaeoenvironmental archive (for e.g. palaeotemperature, palaeosalinity, living habitat) through detailed sampling of the seemingly well-preserved parts for isotope analysis.

Material and methods

For this study, several radiolitid shells were collected from a shallow marine marginal carbonate platform setting in the central Tethys, cropping out today in the east-west oriented Matese Mountain Massif in southern Italy (Monte La Costa (MLC) section; Fig. 2). Based on an integrated bio- and chemostratigraphical framework, the corresponding stratigraphical interval is dated as Early Albian (~ 112 Ma) (Schmitt *et al.* 2019).

Collected shells were screened with a magnifying glass to identify specimens that show the best-preserved visible growth lamellae and minor bioerosion. Subsequently, four very well preserved *Eoradiolitites* shell fragments (A–D) were selected from a 31 m-thick stratigraphical interval, with shell B and D originating from the same interval (MLC 387 m), followed by shell A (MLC 401 m) and shell C (MLC 418 m), which consists of two articulated valves (C1 and C2). Shell A (length: 52.5 mm), B (length: 27.6 mm) and the lower part of C (C2; length: 26.2 mm) represent different ontogenetic stages of the right valve (RV), while the upper part of shell C (C1; length: 13 mm)

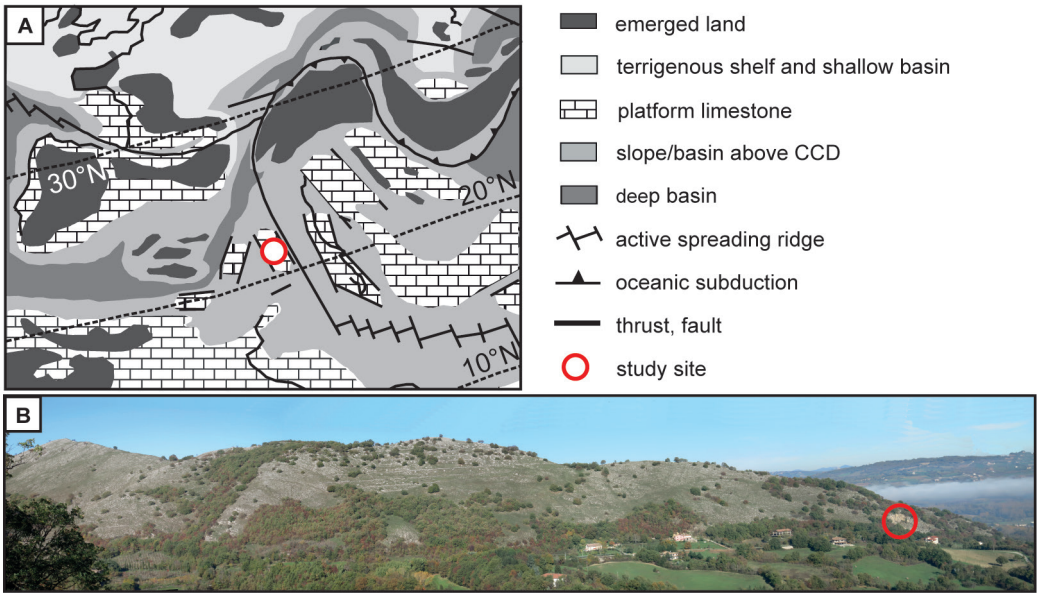

Fig. 2. A, palaeogeographical map of the Late Cretaceous with the studied area of the Apennine Carbonate Platform in the Tethyan realm (modified after Parente *et al.* 2007). B, study site (red circle) in the Matese Mountains, Italy.

and D (length: 59.5 mm) represent portions of the left valve (LV) (Fig. 3). For further information about the lithostratigraphy and the dating, see Schmitt *et al.* (2019).

Selected valves were cut along their perpendicular axis, cleaned with distilled water and dried for 24 h at 40°C. Afterwards, petrographic thin-sections and polished slabs were prepared, which allow to identify changes in the microstructure and to assess sclerochronological changes in isotopic and elemental compositions, respectively. An inner aragonitic layer (a), an inner part of the outer layer (il), an outer layer (bl) and borings were identified in all shell parts (Figs 1, 3). The former aragonitic parts are recrystallized and preserved as blocky diagenetic low-Mg calcite (Fig. 6 G) and are thus excluded from further analyses.

Cathodoluminescence (CL) microscopy was used to investigate the preservation state of collected shell samples. It was applied to polished petrographic thin-sections and slabs using a Reliontron (Relion, USA) cold-cathode luminescence device hosted at the University of Texas at San Antonio (USA). The CL microscope is characterized by an acceleration voltage ranging from 10 to 15 kV and a current intensity ranging from 0.8 to 1.2 mA. The CL chamber was mounted on a Leica DM2700 microscope equipped with 2.5×, 4×, 10× and 20× magnification objectives.

Following petrographic inspections, the elemental composition of the shells was measured by means of a Tornado M4 micro-X-ray fluorescence (μXRF) scanner (Bruker nano GmbH, Berlin, Germany), hosted at the Analytical, Environmental and Geochemistry research group of the Vrije Universiteit (Brussel). The μXRF scanner is equipped with a Rh source and two X Flash 430 Silicon Drift detectors. First, semi-quantitative μXRF-maps were created in order to assess the distribution of major and trace elements across the surface of shell fragments. Polished shell surfaces were scanned in the μXRF mapping mode using a short acquisition time of 1 ms per pixel. Maps were created by focusing the X-ray beam on a circular spot with a diameter of 25 μm and dragging the beam across the polished surface, collecting μXRF spectra every 50 μm in X and Y direction. This procedure yielded ~10^6 μXRF spectra per sample, which allowed semi-quantitative maps of elemental distribution (magnesium, manganese, iron and strontium) to be created based on differences in the area of peaks in the μXRF spectrum associated with elements (ROI counts; see de Winter & Claeys 2016).

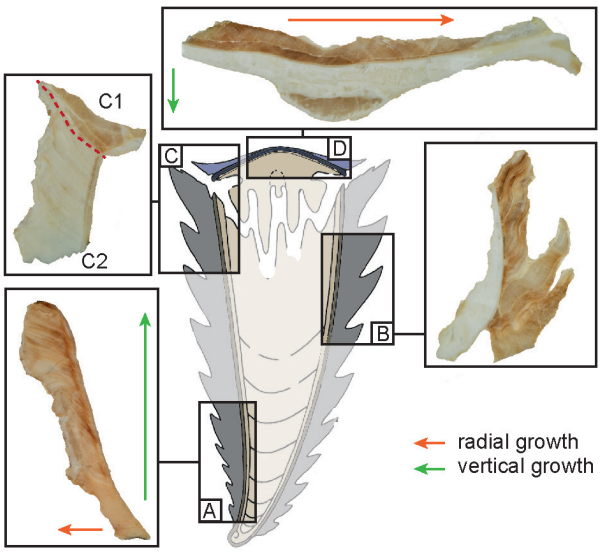

Fig. 3. Schematic representation of a radiolitid shell with the selected shells of this study. A, B, RV; C, articulated LV (C1) and RV (C2); D, LV. Arrows indicate the growth direction of the valves. In the RV vertical (green) dominates radial (red) growth, while in the LV the radial (red) dominates the vertical (green) growth.

Quantitative point-by-point μXRF line scans were performed perpendicular to growth lamellae along the maximum growth axis of each shell fragment with a sampling resolution of 100 μm. Point-by-point line scans allow the X-ray beam to remain on each point for 60 s at maximized energy settings (50 kV, 600 μA, no source filter). This time of analysis represents the ideal compromise between lowering the signal-to-noise ratio (by increasing measurement time) and increasing the spatial sampling resolution (by increasing the number of measurements). This causes the signal-to-noise ratio of individual spectra to be high enough to allow quantification of individual spectra to produce accurate and reproducible measurements of concentrations of a range of major and trace elements (see discussion in de Winter *et al.* 2017b). Therefore, XRF spectra in line scans yield quantitative major and trace element profiles, contrary to spectra of pixels in XRF maps, which can only be used to measure relative changes in element abundances. While concentrations of many elements could be quantified in line scans, only concentrations of strontium (Sr), manganese (Mn), magnesium (Mg) and iron (Fe) are used in this study. The monthly-scale trend was extracted from the trace element profiles by applying a 10-point moving average (see Figs 10–13).

For stable isotope analysis, shells were sampled perpendicular to visible growth lamellae on a sub-millimetre scale. Carbonate powders (~ 150–200 μg) were extracted using a ESI New Wave micromill equipped with a Brassler® USA scriber point carbide drill bit (Ø 0.08 mm). The spacing between the samples was <0.1 mm, similar to the sampling resolution of the μXRF point-by-point line scans. A total of 432 samples

(A: n = 105; B: n = 80; C: n = 39; D: n = 208) were analysed in the stable isotope laboratory of the Institute of Geology, Leibniz University Hannover, Germany using a Thermo Fisher Scientific Gasbench II carbonate device connected to a Thermo Fisher Scientific Delta 5 Advantage isotope ratio mass spectrometer. One hour before the measurements were started, 72°C hot viscous water-free (98 g mol^{-1}) orthophosphoric acid was added to the sample powders, resulting in the release of CO_2. Repeated analyses of certified carbonate standards (per measurement: 3 × NBS 19; 4 × IAEA 603, 4 × NBS 18 and 9 × Carrara Marble) show an external reproducibility (1σ) of ≤ 0.06 ‰ for $\delta^{13}C$ and 0.08 ‰ for $\delta^{18}O$. Isotope ratios are reported as conventional delta values relative to the Vienna-Pee Dee Formation belemnite (VPDB) international standard, in parts per thousand (‰).

Following Steuber's approach (Steuber *et al.* 2005) to facilitate the comparison of the data obtained sea surface temperatures (SST) were calculated using the equation of Anderson & Arthur (1983):

$$T[°C] = 16 - 4.14 * (\delta^{18}O_{C_aCO_3} - \delta^{18}O_{H_2O(seawater)}) + 0.13 * (\delta^{18}O_{C_aCO_3} - \delta^{18}O_{H_2O(seawater)})^2$$

with an estimated $\delta^{18}O_{H_2O(seawater)}$ of –1 ‰ for the Tethys Ocean under ice-free conditions in the Barremian to Campanian (Friedrich *et al.* 2012; Anderson & Arthur 1983; Shackleton & Kennett 1975, Steuber 1996, Steuber & Rauch 2005).

Results

Shell micro- and macrostructures (sclerochronology sensu stricto*)*

On a macroscopic scale, all analysed shell fragments exhibit clearly distinguishable growth lamellae as well as colour variations (transparent to dark brown) (Figs 4 A, 5A, 7A). An exception is the RV shell fragment of C (C2), whose sparite-filled, cellulоprismatic structure produces a significantly lighter colour (Fig. 6 A). Due to their different shell structure, shell fragments were assigned to three categories: (I) non-compact (RV: shells A and B), (II) compact (LV: shells D and C1) and (III) cellulоprismatic (RV: shell C2).

In general, transparent-whitish parts on the shell slabs show non-compact growth lamellae in the thin-sections, visible as blurry, incomplete, wavy and/or not distinguished appearance (dashed black lines in Figs 4 C, 5 C, 7 C). In the non-compact parts, the width of the alternating dark and light growth lamellae is highly variable (their stacking is uneven; Figs 4 E, 5 G). Darker coloured shell parts of the slabs correspond to areas with compact fibrous microstructure in thin-sections (Fig. 7 G, H). Here, cyclic alternations of distinct light and dark, densely packed growth lamellae with an even stacking, are visible (solid black lines in Figs 4C, 5C, 6C, 7C). C2 shows the classical cellulоprismatic structure described in Pons & Vicens (2008) (crosses in Fig. 6 C).

Flame-shaped growth rings (concentric rugae), i.e., arranged lamellae sets, are visible on a macroscopic scale (red dashed line in Figs 1, 5 F). On a microscopic scale, they can be seen due to changes in the inclination of the growth lamellae (Fig. 4 G). A detailed analysis of thin sections revealed that a downwards concentric fold is visible in all RVs, surrounding the recrystallized inner part of the outer layer (il; see Figs 4 F, 5 E, 6 G).

In total, shell fragment A comprises 144 growth lamellae. Only the outermost margin of the lip is formed by a compact fibrous microstructure (Fig. 4 G). Most parts of the shell are characterized by non-compact growth lamellae (Fig. 4 E), but some parts show a very prominent, steep inclination of the lamellae (Fig. 4 D)

Shell fragment B contains 54 growth lamellae characterized by a variable thickness and stacking pattern. The shell exhibits compact structured parts with very prominent, steeply inclined growth lamellae (Fig. 5 E) alternating with non-compact parts, containing a non-distinguishable structure (Fig. 5 G). The outer part of the flame-like shape of the growth rings is often surrounded by a micritic seam. One prominent micrite filled boring trace occurs in the ontogenetically oldest part of the shell (Fig. 5 D).

Shell C comprises in total 130 growth lamellae (C1: n = 22; C2: n = 108). C2 (RV) (Fig. 6 B; grey) shows a mostly regular alternation of growth lamellae and voids, creating a roughly regular radial pattern, which is classified as 'compact with radial elongated voids', following Pons & Vicens (2008; Fig. 6 G). It is further referred to as cellulоprismatic. All cells are filled with blocky calcite. The outer layer (bl) disintegrates at the outer margin of the lip into single cells. At the transition of the valves (C1 to C2) the radial furrow is preserved (Fig. 6 F).

In total, 238 more or less equally distributed growth lamellae were counted in shell D (Fig. 7 G). Occasionally, particularly pronounced growth lamellae appear (Fig. 7 H), which differ from the others due to their very dark colour and higher diameter. Most parts of the shell show a fibrous prismatic structure. Special features of the shell represent borings that are refilled with fine grained micritic calcite (Fig. 7 E).

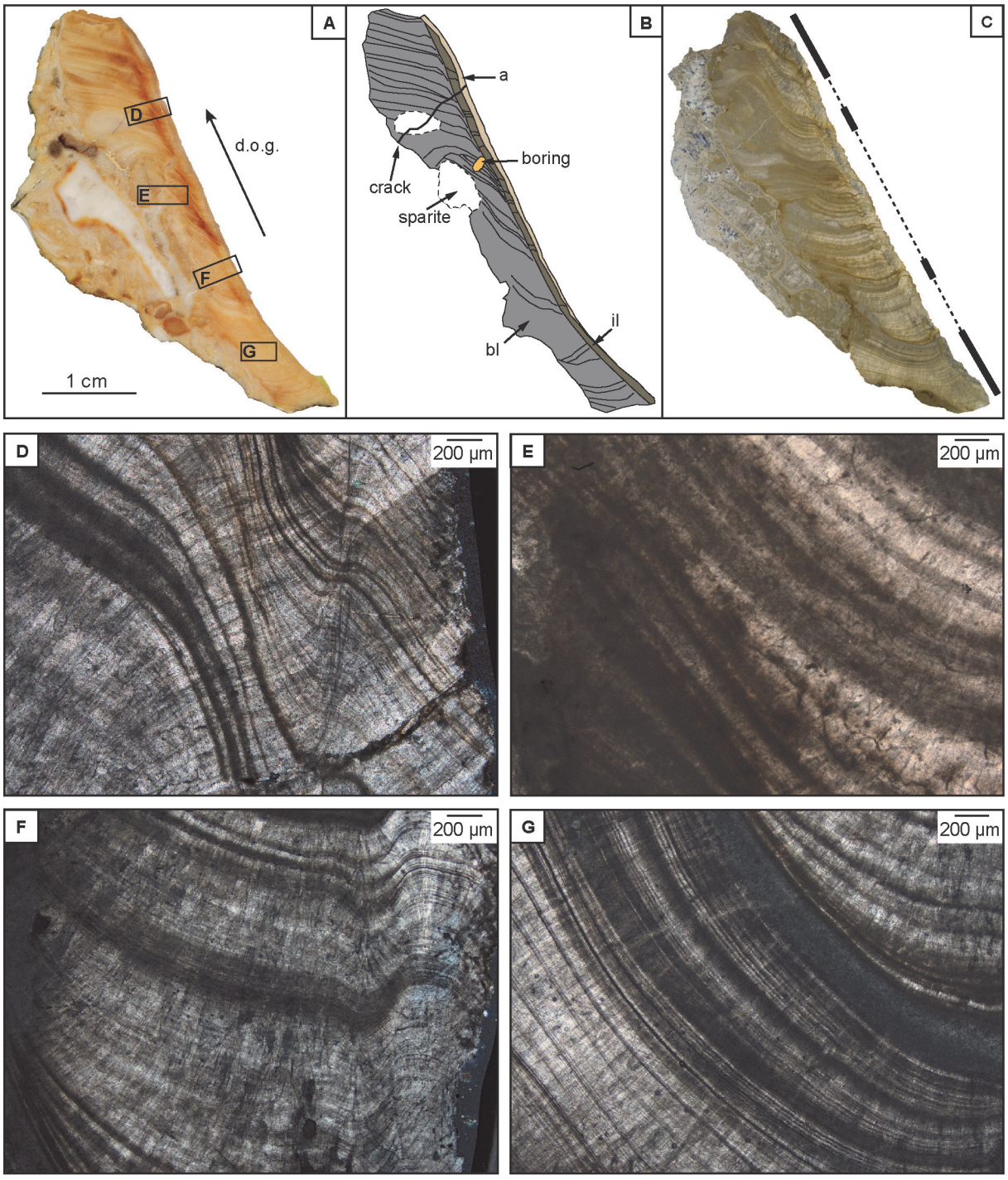

Fig. 4. Shell A (RV). A, image of the slab with areas shown in detailed photomicrographs marked as black boxes. Arrow indicates the direction of growth (d.o.g.). B, schematic sketch and the most important features of the shell: (a) aragonitic layer; (il) inner part of the outer layer; (bl) outer layer and marked crack. C, thin section under plane-polarized light (ppl) with non-compact (dashed line) and compact parts (solid line). D, steeply inclined growth lamellae. E, non-compact growth lamellae. F, detailed view (ppl) showing the transition from the inner part of the outer layer (il; concentric fold) to the outer layer (bl). G, changes in the inclination of the growth lamellae.

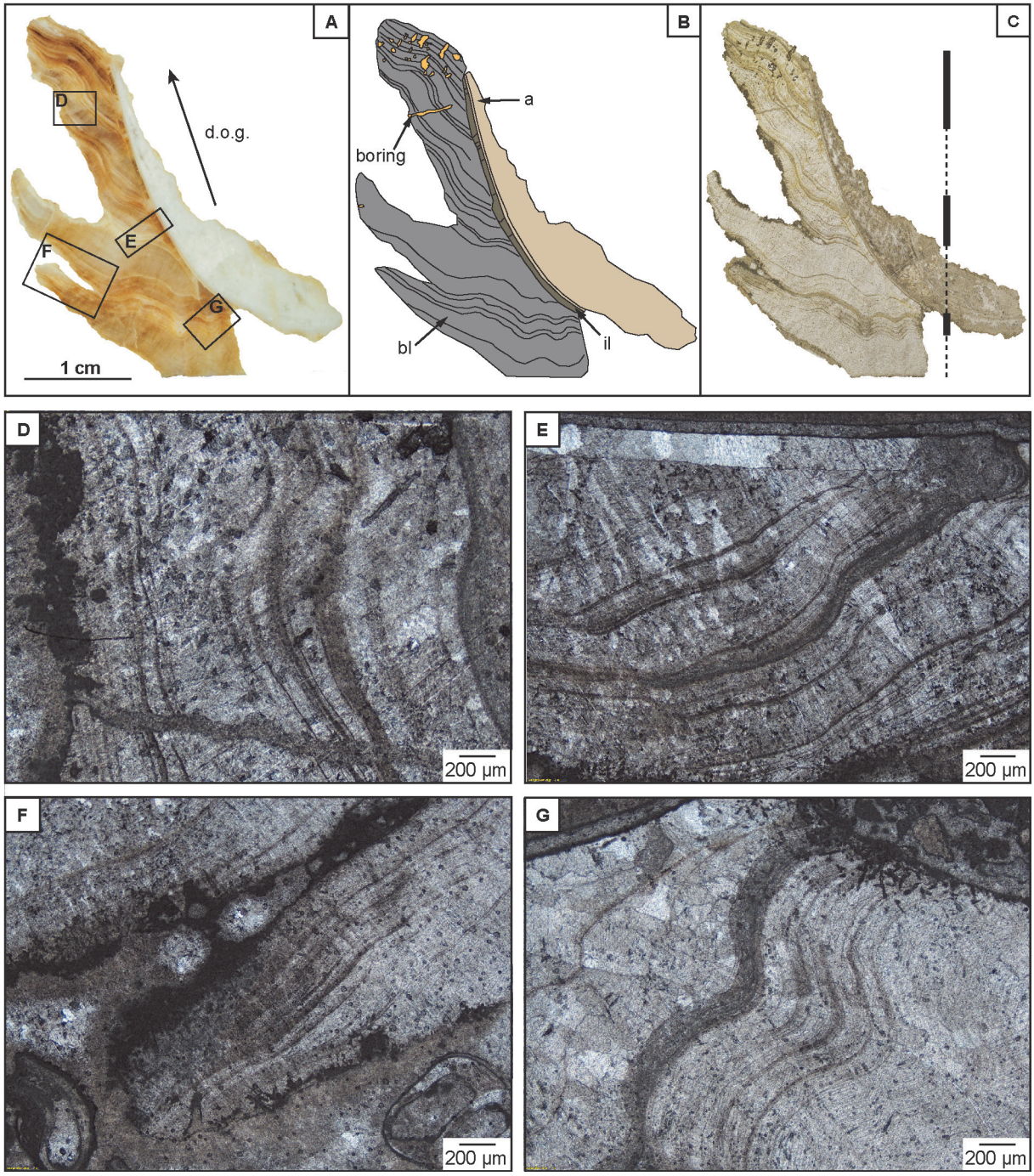

Fig. 5. Shell B (RV). A, image of the slab with areas shown in detailed photomicrographs marked as black boxes. Arrow indicates the direction of growth (d.o.g.). B, schematic sketch and the most important features of the shell: (a) aragonitic layer; (il) inner part of the outer layer; (bl) outer layer and boring. C, thin section (ppl) with non-compact (dashed line) and compact parts (solid line). D, boring filled with micritic calcite. E, steeply inclined growth lamellae and recrystallized inner part of the outer layer (il). F, flame-like shape of growth rings on a macroscopic scale. (G) Variation of expression and the stacking of the growth lamellae.

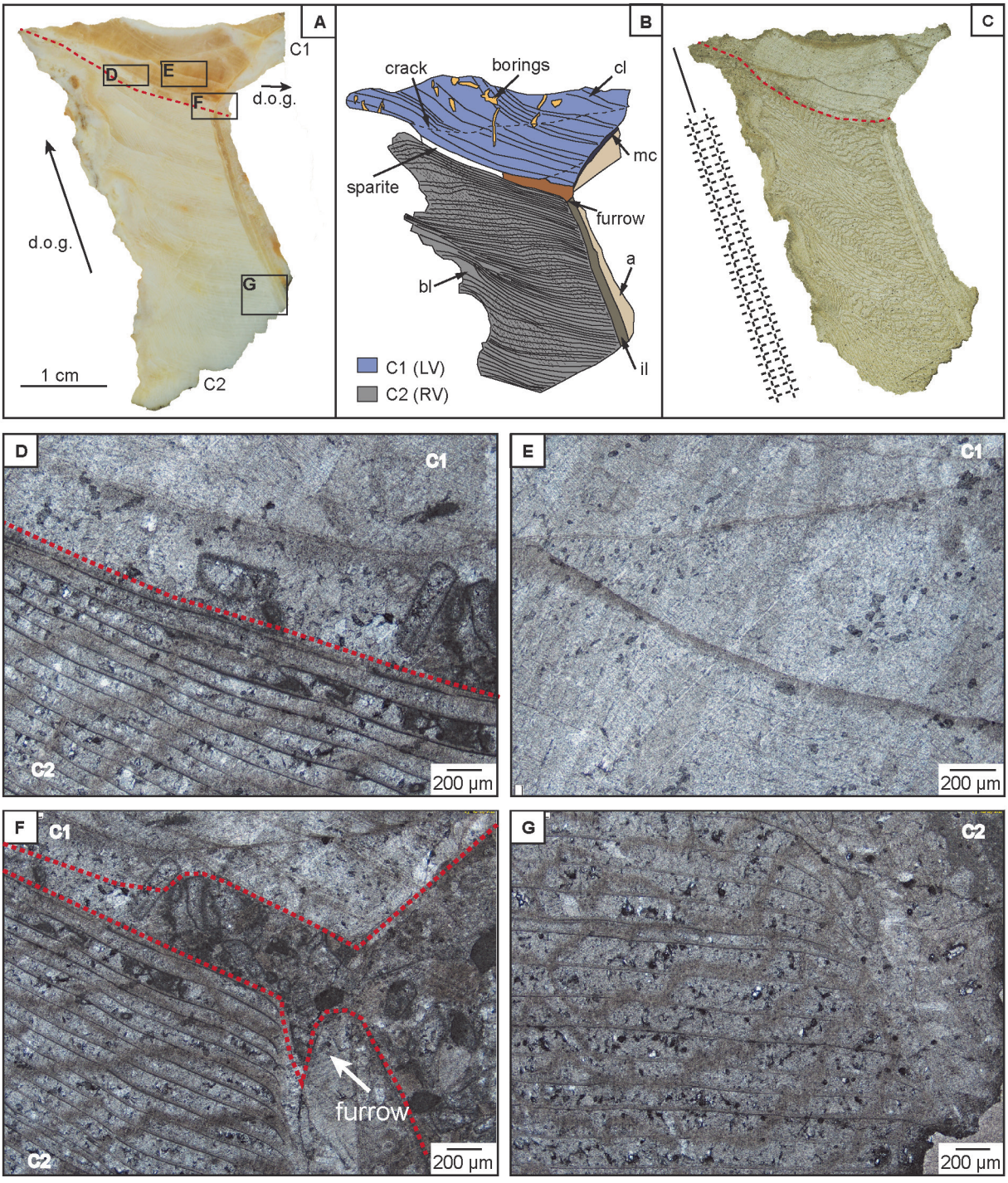

Fig. 6. Shell C is divided (red dashed line) into a left valve (C1) and its articulated right valve (C2). Arrows indicate the direction of growth (d.o.g.). A, image of the slab with areas shown in detailed photomicrographs marked as black boxes. B, schematic sketch and the most important features of shell C. C2: (a) aragonitic layer; (il) inner part of the outer layer; (bl) outer layer. C1: (mc) massive calcite layer; (cl) calcite lamellae, cracks and borings. C, thin section (ppl) with cellulosprismatic structured (cross-hatched double line) in C2 and compact parts (solid line) in C1. D, transition of C1 (LV; compact) and C2 (RV; cellulosprismatic structure). E, compact structure of the C1 (LV). F, transition from the C1 to C2 with furrow. G, detailed view of the cellulosprismatic structure of the outer layer of C2 with recrystallized inner part of the outer layer (il).

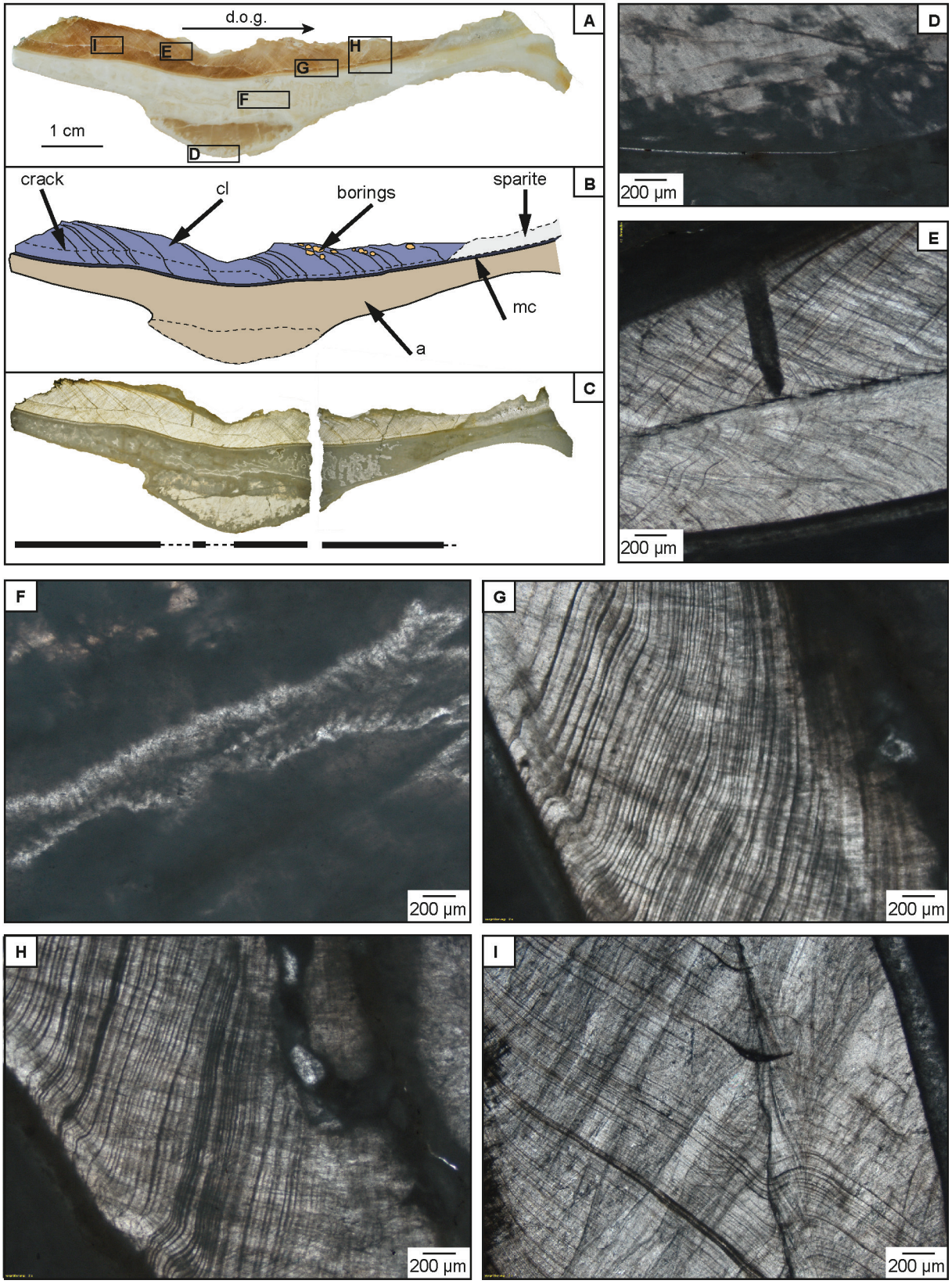

Fig. 7. Shell D (LV). A, image of the slab with areas shown in detailed photomicrographs marked as black boxes. Arrow indicates the direction of growth (d.o.g.). B, schematic sketch and the most important features of the shell. (a) aragonitic layer; (mc) massive calcite layer; (cl) calcite lamellae, crack and borings. C, thin section (plane-polarized light) with blurry (dashed line) and compact parts (solid line). D, lowermost part of the ligament. E, boring. F, middle part of the ligament. G, continuous stacking. H, particularly pronounced growth lamellae. I, changed inclination of the growth lamellae caused by a crack.

Table 1. Identified $\delta^{18}O$ cycles, number of growth lamellae per cycle, distance describes the measured length of the cycles, calculated growth per year (mm) and mean growth lamellae diameter per cycle. Measured maximum and minimum values of $\delta^{13}C$ and $\delta^{18}O$ values and their calculated median. T(°C) was calculated for all $\delta^{18}O$ values.

Sample no	δ18O cycles	number of growth lamellae	distance (mm)	growth per year (mm)	growth lamellae diameter (Ø) in mm	δ13C (‰) Min.	Max.	Median	δ18O (‰) Min.	Max.	Median	T (°C) Min.	Max.	Median
A	1	15	7.6	7.6	48.16	1.80	2.26	2.02	-4.16	-3.35	-3.76	26.4	30.4	28.4
	2	19	15.1	7.4	37.05	1.95	2.64	2.24	-4.14	-3.31	-4.02	26.3	30.3	29.7
	3	14	21.9	6.9	45.06	1.96	2.85	2.30	-4.23	-3.10	-3.79	25.3	30.7	28.6
	4	17	32.6	10.7	59.88	1.85	2.87	2.15	-4.07	-2.93	-3.51	24.5	29.9	27.2
	5	23	39.9	7.3	31.65	2.01	2.87	2.28	-4.06	-2.80	-3.56	23.9	29.9	27.5
	6	28	46.0	6.1	17.55	2.15	3.44	2.53	-3.96	-3.11	-3.63	25.3	29.4	27.8
	7	28	52.5	6.5	25.71	2.52	2.80	2.66	-3.81	-3.12	-3.31	25.4	28.7	26.3
		Σ 144		**Σ 52.5**										
B	1	1	3.5	3.5	124.81	0.93	2.02	1.38	-4.29	-3.15	-4.00	25.5	31.0	29.6
	2	10	10.7	7.2	47.26	1.60	2.43	1.88	-4.35	-2.91	-3.69	24.4	31.3	28.1
	3	24	24.3	13.7	42.66	1.61	2.48	1.89	-4.31	-3.13	-3.48	25.4	31.1	27.1
	4	7	27.5	3.2	37.94	2.16	2.26	2.21	-3.73	-3.06	-3.40	25.1	28.3	26.7
		Σ 42		**Σ 27.6**										
C	C1	22	39.3	8.6	55.52	1.93	2.88	2.49	-4.88	-3.54	-3.84	27.8	34.0	28.8
	C2	108	31.3			1.97	2.49	2.25	-4.86	-1.44	-2.62	17.8	33.9	23.0
		Σ 130		**Σ 39.2**										
D	1	51	10.8	10.8	22.42	1.11	1.55	1.39	-4.24	-3.87	-4.03	29.0	30.8	29.7
	2	83	30.3	19.5	21.39	0.89	2.05	1.46	-4.74	-2.52	-3.63	22.6	33.3	27.8
	3	95	53.4	23.1	31.31	1.01	1.89	1.46	-4.48	-2.93	-3.65	24.5	32.0	27.9
	4	9	59.5	6.1	76.72	1.55	1.93	1.67	-4.01	-3.50	-3.77	27.2	29.6	28.5
		Σ 238		**Σ 59.5**										

At some parts the shell margin is micritized. All sclerochronological results are summarized in Table 1.

Elemental and isotope compositions

CL was applied to all three shell structures (Fig. 8 A–C). Compact shell portions show a dim, orange luminescence between single growth lamellae. Growth lamellae themselves are non-luminescent (Fig. 8 D). Within non-compact (Fig. 8 E) and celluloprismatic structures (Fig. 8 F) dark brown to light orange CL colours provide evidence for various cement generations.

µXRF element mapping provided valuable information with respect to the preservation state of considered shells. Inclusions with higher concentrations of Fe and Mn indicate recrystallized or bioeroded parts (borings) of the shells. All shells contain strontium, but the concentration varies considerably depending on the shell structure. For example, the compact parts of the LV (Fig. 8 H C1, J) have a significantly higher Sr concentration than the non-compact parts (Fig. 8 G, I) or the celluloprismatic parts (Fig. 8 H C2,) of the RVs. Especially in the latter one the Sr content is very low.

Due to the high resolution of the point-by-point µXRF line scans measured at the micrometre scale resolution, the data sets were filtered to reduce the impact of analytical outliers and irregularities that occurred in the shell (e.g. boreholes or cracks). Therefore, following Steuber (1999), ranges indicating trace element composition of pristine calcite with low Mg content were defined (Sr: 900 to 1500 µg/g; Mn: < 200 µg/g; Fe: < 300 µg/g). All data points that were not within the defined thresholds were excluded from further analysis. In addition, cross plots were used to separate outliers (Fig. 9). Finally, a 10-pt average was calculated. The raw data and selected values are shown in Table 2.

The uncertainty of the µXRF results was quantified in three ways to illustrate the sources of error in the trace element analyses used in this study (Table 3). Firstly, the uncertainty on moving averages was quantified along shell profiles by calculating the 95 % confidence interval on the pooled standard deviation of variability within each group of 10 points which are averaged in XRF profiles to arrive at a pooled 95 % confidence interval of precision for each element in the trace element dataset. This method includes both

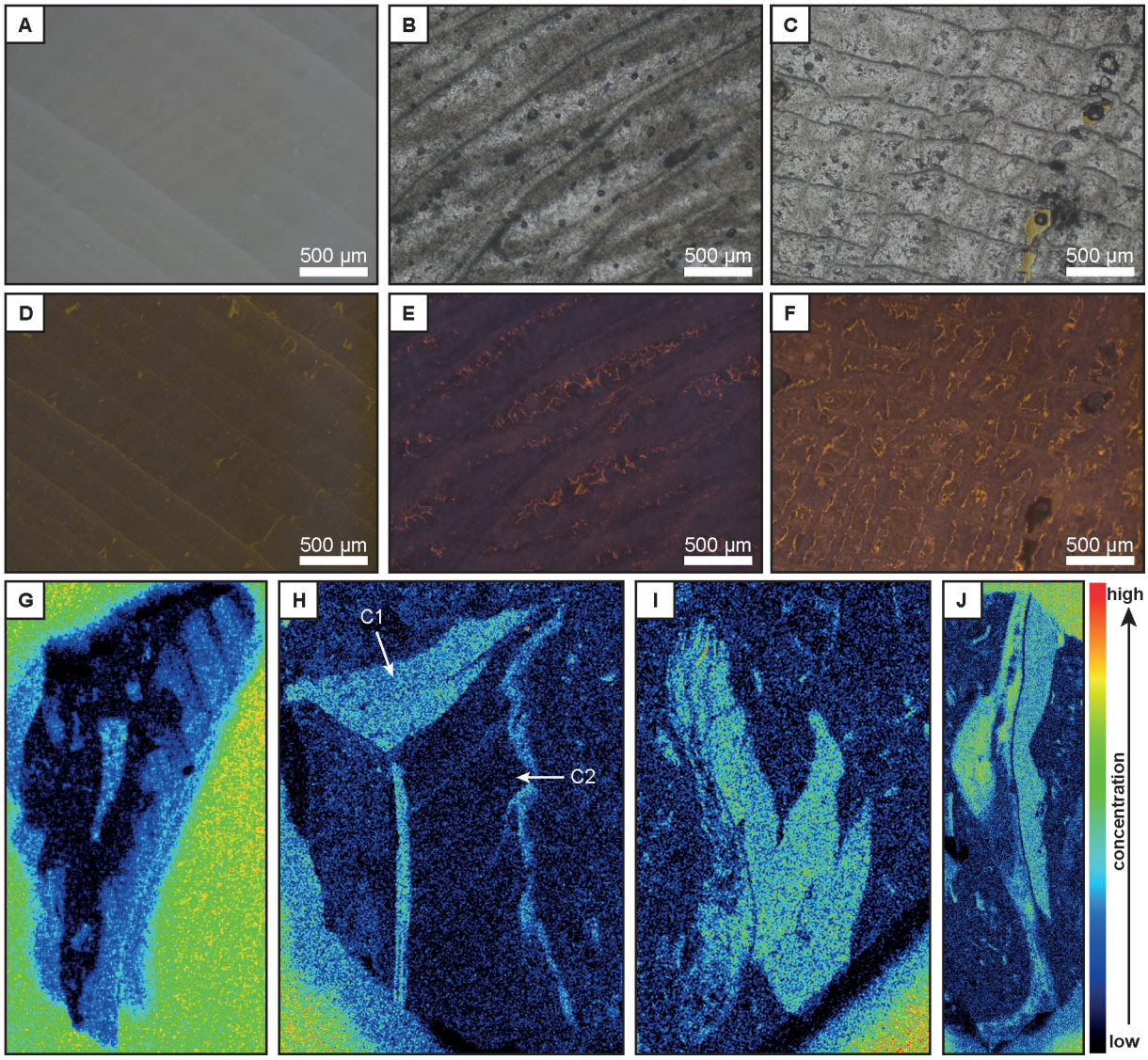

Fig. 8. A, image of a polished slab of a compact shell part (shell A). B, petrographic thin sections of non-compact parts under ppl (shell A). C, petrographic thin sections of a celluloprismatic structure under ppl (Shell C2). D, CL image of a compact shell part with only a weak, orange luminescence between the individual growth lamellae. E, CL images of a non-compact part, where different CL colours (brown to light orange) demonstrate that different generations of cement exist. F, CL images of celluloprismatic structures with light orange CL colours. G–J, variations in Sr concentration in the µXRF maps. The Sr concentration is lowest in C2 (H, celluloprismatic structured RV) and highest in shell D (J, compact LV).

measurement uncertainty and small-scale variability in the shell itself into uncertainty estimates and therefore likely overestimates measurement uncertainty. This method results in typical 95 % confidence levels of uncertainty for Mg (±396 µg/g), Sr (±35 µg/g), Mn (±50 µg/g) and Fe (±45 µg/g) Secondly, the accuracy of the calibration of the XRF data was quantified by propagating the standard error on the slope of the calibration onto the mean concentration of each element in the trace element dataset. This error analysis likely underestimates the full uncertainty of XRF analyses, as it does not consider the uncertainty on the measurement procedure itself, only the calibration accuracy. Following this method results in uncertainty standard deviations for Mg (±53 µg/g), Sr (±1.5 µg/g), Mn (±2.6 µg/g) and Fe (±1.6 µg/g). Thirdly, the standard deviation on repeated measurements (n = 10) was calculated on three powdered homogenized carbonate reference materials (BAS CRM393 & CRM513; Bureau of Analysed Samples, Middlesbrough, UK and NIST SRM1d; National Institute of Standards and Technology, Gaithersburg, MD, USA). Note that the concentrations of the elements of interest for this study (Mg, Sr, Mn and Fe) in these standards is not

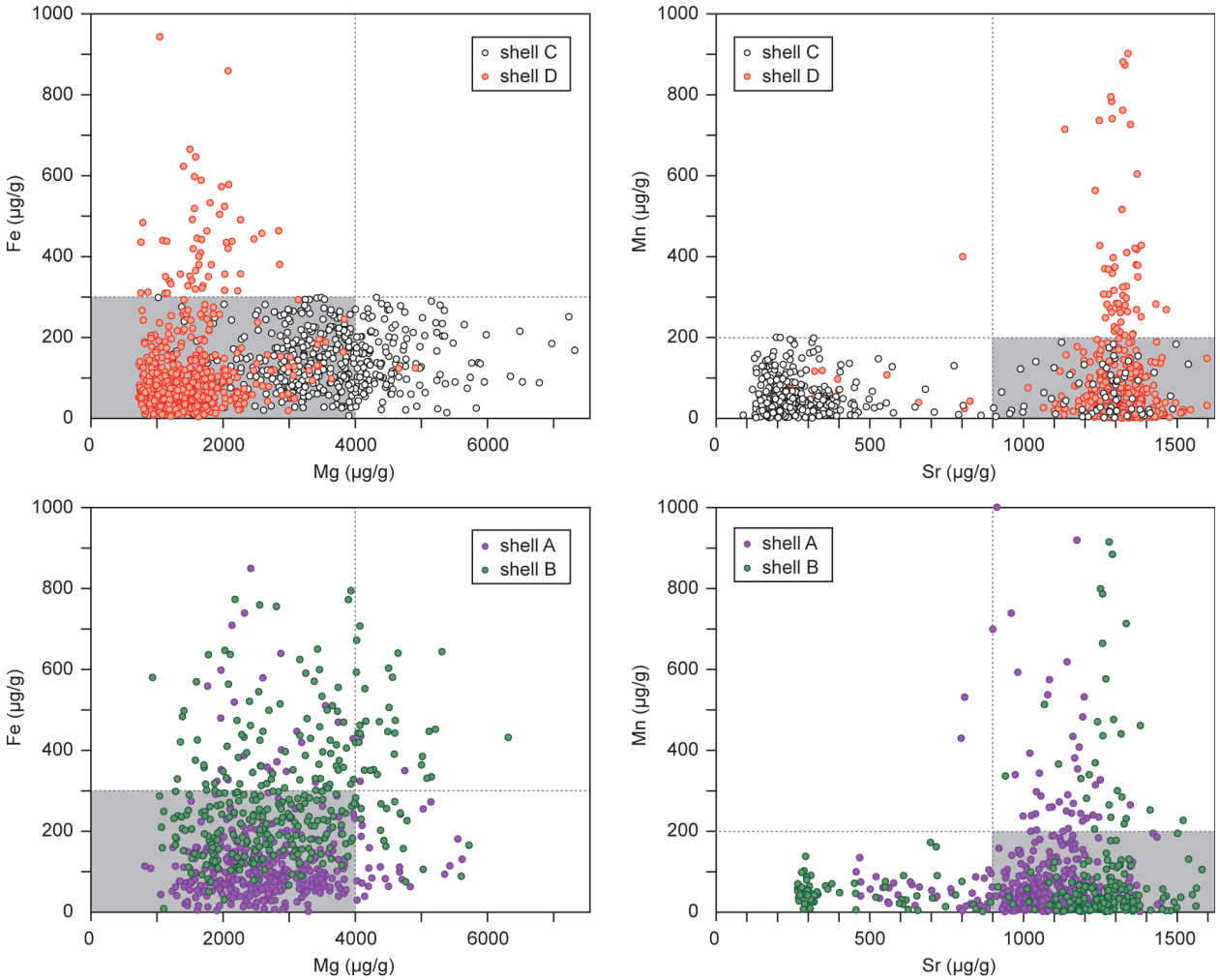

Fig. 9. Fe vs. Mg and Mn vs. Sr of the here analysed shells. Due to their clustering thresholds were assumed: Sr 900–1500 µg/g, Fe: < 300 µg/g, Mn < 200 µg/g for further analysis. For Mg, no threshold was applied as the data points scatter widely.

Table 2. Elemental compositions (µg/g) of selected low-Mg carbonate rudist shells of the Monte La Costa section before (a) and after (b) the thresholds were applied. Data provided in (b) are the basis for further analysis.

Sample no		Sr (ug/g)			Fe (ug/g)			Mn (ug/g)			Mg (ug/g)		
		Min.	Max.	Mean	Min.	Max.	Mean	Min.	Max.	Mean	Min.	Max.	Mean
a	A	456	1448	1058	2	848	130	0	531	81	826	5628	2697
	B	266	1582	1085	8	1307	288	0	914	89	942	6327	2907
	C	88	1537	462	6	299	145	0	200	52	976	8501	3674
	D	241	1902	1283	1	942	126	0	1329	101	737	4921	1548
b	A	933	1350	1102	37	191	92	0	156	48	1669	4923	2587
	B	924	1435	1239	132	267	199	0	111	45	1004	3520	2260
	C	161	1425	487	75	247	145	0	110	47	1661	4835	3018
	D	1118	1495	1313	25	274	92	0	186	49	1074	2300	1459

Table 3. Results of analysing uncertainty of micro-XRF results on rudist calcite using three different statistical methods.

Element	Method	Mg (ug/g)	Sr (ug/g)	Mn (ug/g)	Fe (ug/g)
Average (ug/g)	-	2594	1118	70	97
Reproducibility within moving averages (95% CL)	1	396	35	58	45
Calibration uncertainty (SE slope)	2	53	1	3	2
Reproducibility within CRM393 carbonate standard (SD)	3	274	6	85	3
Reproducibility within CRM513 carbonate standard (SD)	3	256	18	30	8
Reproducibility within SRM1d carbonate standard (SD)	3	240	19	1590	9

always similar to that of the rudist shells analysed for this study, and therefore the outcome of this precision analysis may not be fully representative of the trace element results in this study. The uncertainty standard deviations according to this method on the CRM393 standard, which most closely resembles the shells in terms of composition, are: ±274 µg/g for Mg, ±6 µg/g for Sr, ±85 µg/g for Mn and ±8 µg/g for Fe.

The resulting smoothed trace element profiles exhibit significant (> 2 SD, see Tab. 3) millimetre scale variability in Mg, Sr, Mn and Fe concentrations (Figs 10–13). In general, Mn and Sr concentrations seem to fluctuate at the same scale as stable isotope profiles (period of roughly 10 mm in Fig. 10 or 20 mm in Fig. 13), with Sr and Mg contents varying in antiphase (see Fig. 11). Variability in Mn and Fe concentration has a 2–3 times shorter period compared to Mg and Sr and seems to show no apparent correlation with each other or with the isotope profiles.

Oxygen isotope values of shell A (Fig. 10) vary between –2.8 ‰ and –4.2 ‰, whereas carbon isotope values range from 1.8 ‰ to 3.4 ‰. In total, five $\delta^{18}O$ cycles with amplitudes of < 1 ‰ were identified, showing either a periodic triangular or a saw tooth

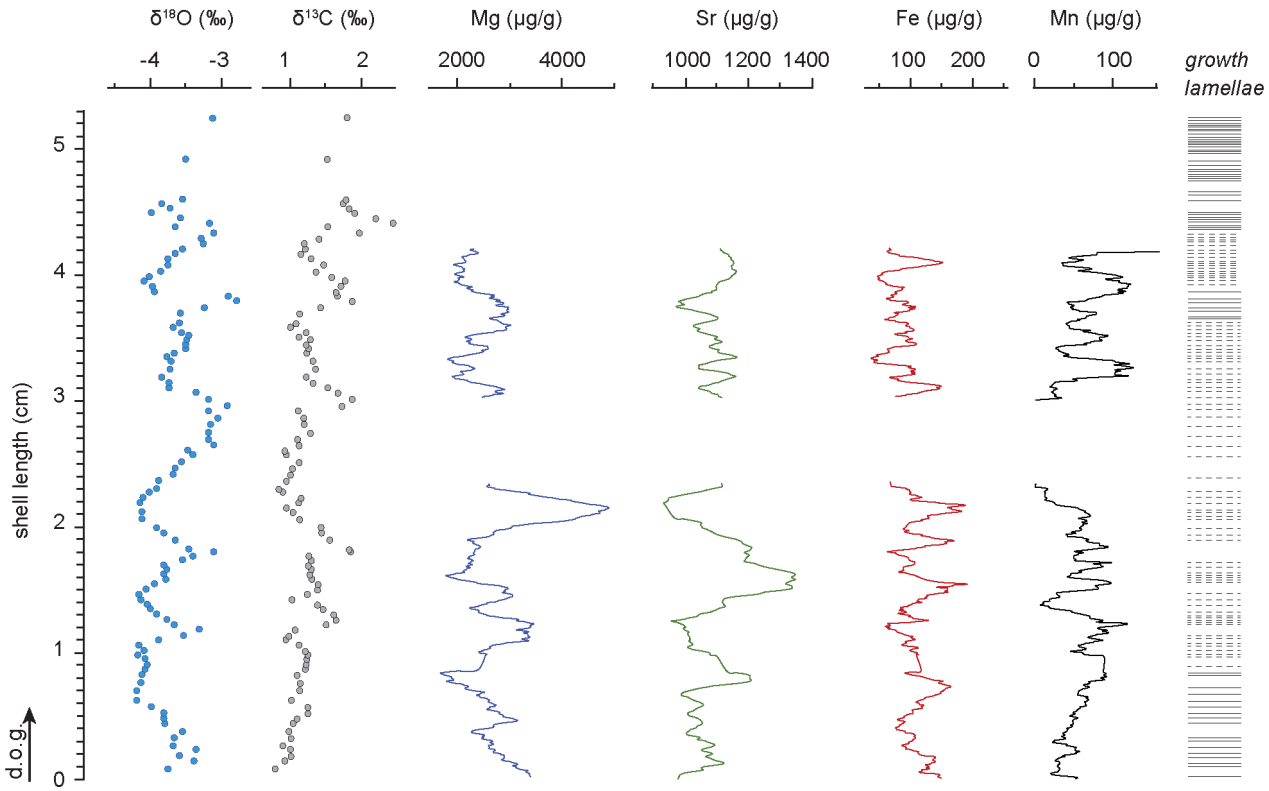

Fig. 10. Oxygen and carbon isotopic composition with Sr, Fe, Mn and Mg variations plotted against the identified and counted growth lamellae of shell A. Dashed lines show the non-compact shell structure parts, solid lines show compact parts.

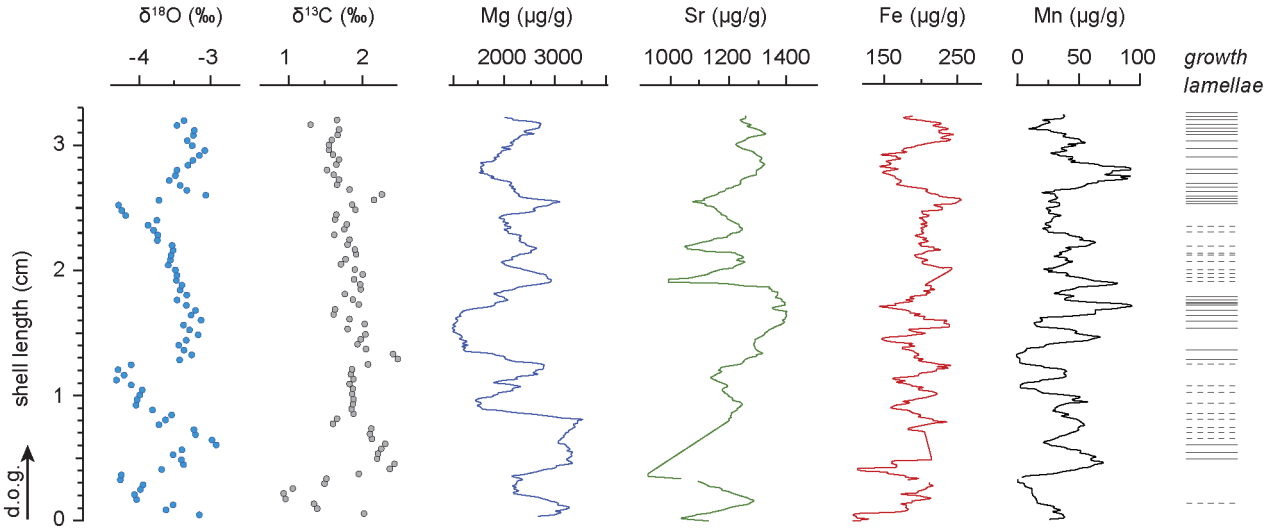

Fig. 11. Oxygen and carbon isotopic composition with Sr, Fe, Mn and Mg variations plotted against the identified and counted growth lamellae of shell B. Dashed lines show the non-compact shell structure parts, solid lines show compact parts.

shape (Fig. 10). These five cycles are also visible in the carbon isotope record. These superimposed rapid changes towards more positive $\delta^{13}C$ values weakly correlate with corresponding positive shifts in $\delta^{18}O$ (Fig. 10: 1.2–4.5 cm; $r^2 = 0.2$). µXRF line scanning provides evidence for periodic changes in Mg concentrations (period: 0.3–0.6 cm), ranging from 1700 to 3500 µg/g. An exception from this pattern is a prominent positive spike reaching Mg concentrations of 4900 µg/g (Fig. 5: 2.1 cm). Sr concentrations fluctuate between 930 µg/g and 1100 µg/g. Significantly higher amounts of Sr (< 1350 µg/g) are recorded in the lower third of the shell (Fig. 10: 1.3 to 1.8 cm). Fe concentrations are highly variable (40 µg/g to 190 µg/g), with values oscillating around a mean value of about 90 µg/g. Mn concentrations range from 0 µg/g to 160 µg/g, exhibiting a superimposed cyclic pattern with higher frequency in the upper part of the shell (Fig. 10: 3–4.2 cm).

Oxygen isotope values of shell B (Fig. 11) vary between –2.9 ‰ and –4.4 ‰, whereas carbon isotope values range from 0.9 ‰ to 2.5 ‰. Identified $\delta^{18}O$ cycles (n = 2) exhibit a triangular to sinusoidal shape with a mean amplitude of 1.3 ‰ and a wavelength of 0.7 cm and 1.4 cm, respectively (Fig. 11). Gradually decreasing values characterizing the second cycle are likely explained by a slightly oblique cut through growth lamellae. Carbon isotope values lack a similar cyclic pattern and fluctuate around a background value of about 1.6 ‰. In the lower part of the shell (Fig. 11: 0.3–1.2 cm), however, rapid negative and positive shifts in $\delta^{13}C$ correlate well with corresponding shifts in $\delta^{18}O$ ($r^2 = 0.4$). Mg concentrations are characterized by periodic fluctuations (wavelength: 0.2–0.5 cm; amplitude: 1000 µg/g to 2000 µg/g) that are superimposed on a cyclic sinusoidal pattern with a range from 1004 to 3520 µg/g. Sr concentrations range from 924 µg/g to 1435 µg/g (mean value: 1239 µg/g) and provide evidence for a cyclic pattern. Fe concentrations exhibit a short term cyclicity (132 µg/g to 267 µg/g), with values oscillating around a mean value of 199 µg/g. Mn concentrations show a cyclicity (5 µg/g to 111 µg/g), with values oscillating around 45 µg/g.

Oxygen isotope values of shell C (Fig. 12) vary between –1.4 ‰ and –4.9 ‰, whereas carbon isotope values range from 1.9 ‰ to 2.9 ‰. In total, the values derived from C2 (RV) are highly variable, while the values of C1 (LV) show one broadly symmetrical sinusoidal $\delta^{18}O$ cycle with an amplitude of <1.3 ‰ (Fig. 12). The $\delta^{13}C$ values of C2 oscillate within a range between 1.9 to 2.4 ‰. No clear pattern is observed. The $\delta^{13}C$ values of C1 oscillate within a range between 2.2 to 2.7 ‰. µXRF line scanning of Mg of C2 shows a highly variable record with oscillations of ~ 500 µg/g, while C1 provides evidence for periodic changes in Mg concentrations (wavelength: 0.2–0.4 cm), the latter ranging from 1700 to 4600 µg/g. The Sr concentrations of C2 fluctuate between 160 µg/g and 260 µg/g, while C1 contains a significantly higher amounts of Sr (range: 920–1430 µg/g) with cyclic oscillations (0.4 cm wavelength) (Fig. 12). Fe concentrations provide evidence for a small scale cyclicity (80 µg/g to 250 µg/g), with values oscillating around a mean value of about 150 µg/g. Significant differences between the valves cannot be observed. Mn concentrations range from 0 µg/g to 110 µg/g, exhibiting a superimposed cyclic pattern with wavelengths oscillating around 0.3 cm (Fig. 12).

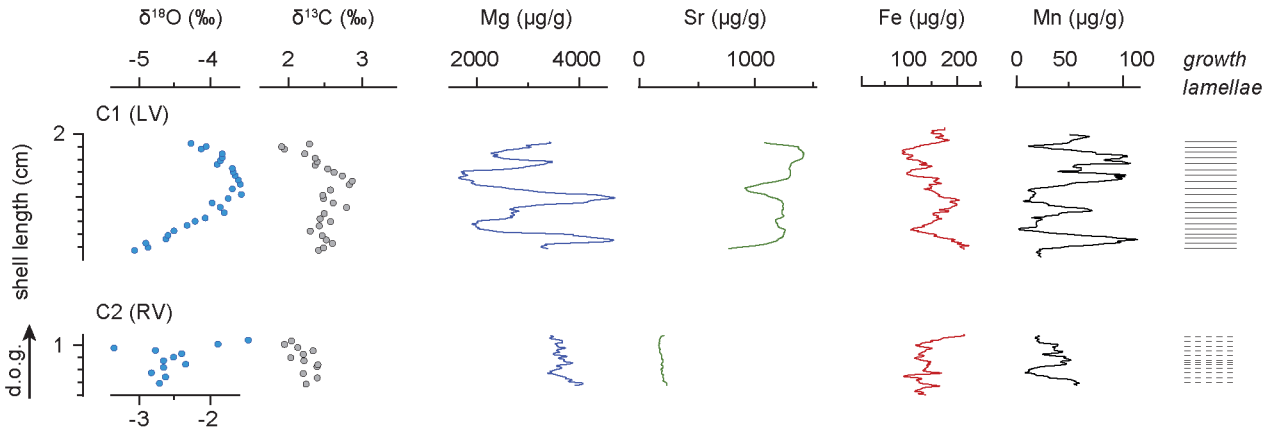

Fig. 12. Oxygen and carbon isotopic composition with Sr, Fe, Mn and Mg variations plotted against the identified and counted growth lamellae of shell C. Dashed lines show the non-compact shell structure parts, solid lines show compact parts.

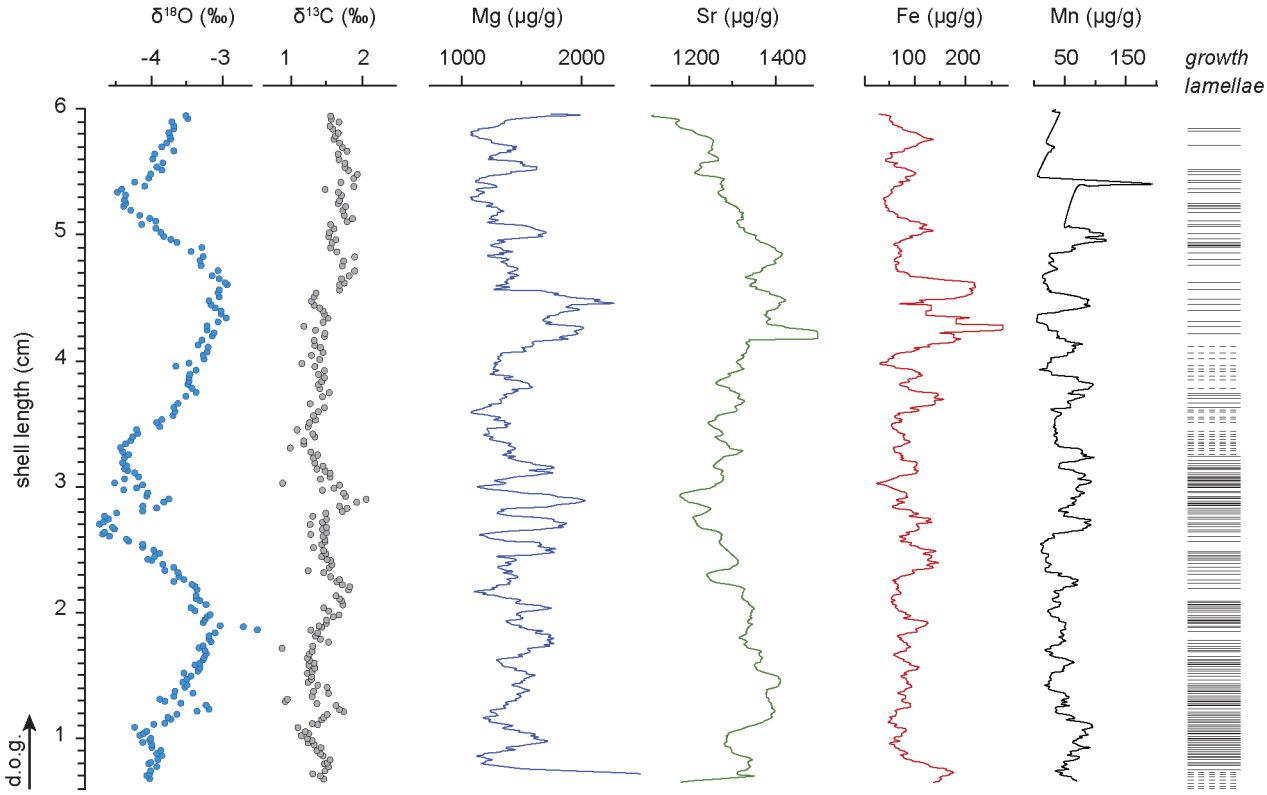

Fig. 13. Oxygen and carbon isotopic composition with Sr, Fe, Mn and Mg variations plotted against the identified and counted growth lamellae of shell D. Dashed lines show the non-compact shell structure parts, solid lines show compact parts.

Oxygen isotope values of shell D (Fig. 13) vary between –2.5 ‰ and –4.7 ‰. Carbon isotope values range from 0.9 ‰ to 2.0 ‰. In total, two prominent $\delta^{18}O$ cycles with amplitudes of <1.7 ‰ were identified, showing a broadly symmetrical sinusoidal pattern (Fig. 13). Most $\delta^{13}C$ values oscillate around 1.5 ‰. Superimposed rapid changes in $\delta^{13}C$ towards more positive values correlate strongly with corresponding positive shifts in $\delta^{18}O$ (Fig. 13: 1.1–1.4 cm: $r^2 = 0.6$ and 2.8–3.1 cm: $r^2 = 0.8$). Mg concentrations are highly variable (1100 to 2300 µg/g). Sr concentrations are positively correlated with $\delta^{18}O$ values, expressed by two symmetrical sinusoidal cycles. Concentrations range from 1120 µg/g to 1500 µg/g. Fe concentrations

show small scale cyclic changes, with values varying from around 30 µg/g to 270 µg/g. Mn concentrations show a highly fluctuating record with a range from 0 µg/g to 190 µg/g.

Discussion

Preservation state

Rush & Chafetz (1990) demonstrated with their study of Palaeozoic brachiopod shells that the preservation of original microstructures does not necessarily exclude any diagenetic changes in the isotopic composition of the shells. The best way to reliably assess the preservation of the studied shells is the combination of petrographic (CL and µXRF mapping) and geochemical methods (IRMS and µXRF line scans).

Petrographic analyses.- Areas of the shells with a clearly visible alternation of light to dark lamellae, i.e., in the compact areas (shell C1, D but also in some parts of shell A and B) do not show signs of strong diagenetic overprint under transmitted light and CL (Figs 4–8). This observation is supported by XRF mapping (Fig. 8 G, J), which shows high Sr concentrations in the corresponding shell structures. In contrast, non-compact parts of shells A and B show clear evidence of diagenetic alteration under transmitted light and CL microscopy (Fig. 8 A–F). This can be well explained by the higher primary porosity of these shell parts, enabling circulation of diagenetic fluids (Regidor-Higuera et al. 2007). The cellulоprismatic parts show evidence of diagenetic alteration, which is clearly visible through orange-red luminescence under CL (Fig. 8 F). Compared to the non-compact parts, primary porosity in the cellulоprismatic shell parts was significantly higher, allowing fluids to circulate through these structures more easily. The porosity decreased over time as secondary calcite precipitated (Regidor-Higuera *et al.* 2007).

Elemental dataset.- Considering the elemental data, it is generally assumed that samples are diagenetically altered if the Mn and Fe concentrations in the sample increase coupled with decreasing (Mg and) Sr concentrations (Brand & Veizer 1980; Al-Aasm & Veizer 1982; Steuber 1999). The change in Mn and Fe, which might be caused by ontogenetic effects cannot yet be estimated, so here the Mg/Sr ratio is used to detect diagenesis (Veizer 1983; Steuber 1999). Using this criterion, a cross-plot (Fig. 14) reveals that shells A, B, C1 and D which are composed predominantly of compact and non-compact shell structures,

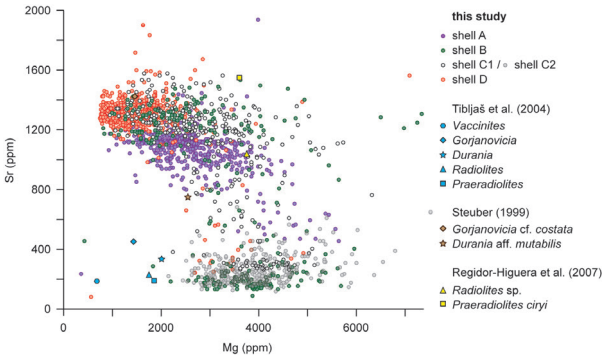

Fig. 14. Mg and Sr compositions of rudist shell A (purple), B (green), C1 (white), C2 (grey) and D (red) compared with radiolitids from Croatia (Tibljaš et al., 2004), Greece, United Arab Emirates (Steuber 1999) and Spain (Regidor-Higuera *et al.* 2007).

contain a high Sr concentration value coupled with a highly variable Mg concentration. These shells are in a range similar to the rudist shell material classified as well-preserved from the studies by Steuber (1999) and Regidor-Higuera *et al.* (2007). However, various data points of shell B and C2 show low Sr values coupled with Mg concentrations, that are higher compared to the ones from shell A, B, C1 and D (Fig. 14), which might be linked to variations in metabolic activity (Rosenberg & Hughes 1991, Klein *et al.* 1996), kinetic fractionation (Carpenter & Lohmann 1992) or which is interpreted in the case of the cellulоprismatic structure to represent diagenetically altered calcite (Al-Aasm & Veizer 1986a, b; Steuber 1999; Tibljaš *et al.* 2004). It is assumed that these values result from the infill of the former hollow structures with secondary cement (Regidor-Higuera et al. 2007). However, diagenetic alteration can only be partially confirmed for shell C2. Low Sr concentrations (< 200 µg/g) could indicate diagenetic alteration, but very high Mg values (3500–4000 µg/g) do not seem to confirm this, as diagenetic altered calcite typically contains less Mg, and rudist shell calcite is naturally low in Mg (Al-Aasm & Veizer 1986a, b; Steuber 1999; Tibljaš *et al.* 2004).

Mg concentrations and Mg/Ca ratios in marine calcifiers are strongly influenced by calcification temperature (e.g. Klein *et al.* 1996; Steuber 1996; Elderfield & Ganssen 2000; Watanabe *et al.* 2001; de Winter *et al.* 2017a). However, the application of the Mg/Ca thermometer in bivalve carbonate is problematic, as metabolic effects have been demonstrated to influence shell Mg/Ca and Sr/Ca ratios in modern species (e.g. Freitas *et al.* 2006; Steuber *et al.* 2011). The higher order (sub-seasonal) variability in Mn and Fe resembles short-lived changes in the concentrations of these elements in modern mollusc shells related to

sub-annual changes in redox condition, tidal rhythms and storm activity (Freitas *et al.* 2006; Marali *et al.* 2017; Huyghe *et al.* 2019; Yan *et al.* 2020). While the precise palaeoenvironmental interpretation of these high-resolution trace element records requires a more detailed understanding of the mineralization in mollusc shells at the sub-annual scale, the preservation of fine scale trace element patterns in non-compact and compact shell sections of *Eoradiolites* highlights the potential of these rudists as archives for short-term (sub-seasonal) environmental change in Mesozoic shallow marine environments (see e.g. de Winter *et al.* 2020).

Isotopic dataset.- Non-compact parts, observed in the RVs of shells A (Fig. 10) and B (Fig. 11), show sharp shifts towards more positive $\delta^{18}O$ values. However, the presence of non-compact shell structures (which were assumed to be diagenetically altered) does not automatically indicate the absence of any primary signatures, as the low correlations of $\delta^{13}C$ and $\delta^{18}O$ values and the quasi sinusoidal $\delta^{18}O$ pattern suggest. Furthermore, the $\delta^{18}O$ values in the RVs are similar to those derived from the LVs and are in turn comparable to previous $\delta^{18}O$ measurements from well-preserved low-Mg calcite outer shell layers of hippuritid rudists (Steuber 1999).

Shell fragments characterized by a compact structure provide oxygen isotope values with a smooth sine function pattern, as visible in shell D (Fig. 13) and C1 (Fig. 12), both LVs. This distinct pattern is interpreted to mirror seasonal changes, without any significant growth cessations. The cellulоprismatic structure of C2 (Fig. 12) shows a highly variable $\delta^{18}O$ pattern, lacking clear cyclic variations. Seasonality cycles are not identifiable, probably due to the infill of the cellulоprismatic structure with secondary calcite. The lack of a clear seasonal pattern could also result from the limitation of data points measured within this structure.

Although individual sclerochronological patterns are varied, all shells show an almost identical range of $\delta^{18}O$ values (Tab. 1). Cyclic variations of $\delta^{13}C$ and $\delta^{18}O$ observed in shell A show a covariance, which is slightly out of phase (Fig. 10). Despite previous studies proposing correlations between $\delta^{13}C$ and $\delta^{18}O$ as indicative of kinetic processes associated with diagenetic recrystallization (e.g. Al-Aasm & Veizer 1986b) this is not necessarily a sign for diagenetic alteration in the here analysed shells. Cross-plots and R^2 values derived from the whole dataset reveal a low (shell A, B, C1), absent (shell D), and moderate (shell D) correlation of isotope values (Fig. 15). The $\delta^{13}C$ variations are supposedly caused by seasonal variations

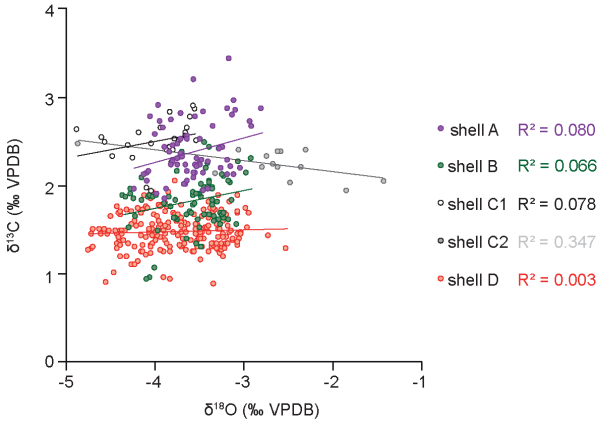

Fig. 15. Cross-plot of $\delta^{18}O$ and $\delta^{13}C$ of the studied shells and their correlation factor (R^2).

in marine productivity and its effects on marine dissolved bicarbonate (Arthur *et al.* 1983; Steuber 1996).

Estimating radiolitid growth rates

In general, annual cycles preserved in rudist shells can be determined using: (1) flame-shaped growth rings (concentric rugae); (2) changes in the microstructure of the shell; or (3) cyclic repetition in the isotopic $\delta^{18}O$ pattern. Growth rates of radiolitid rudists can be estimated using the number of lamellae per determined annual cycle. Schumann (1995) proposed that a complete "annual" cycle includes 24–25 growth lamellae. However, Regidor-Higuera *et al.* (2007) state that the number, the width, the stacking and the structure of lamellae per year can vary between different genera and species, depending on the environment in which the shell was built.

In this study all three methods were applied: (1) annual cycles were determined via growth ring inspection on a macroscopic scale in shell B; however, this approach is often unfeasible, since the flame-like structure is very fragile and therefore often absent due to the reworking of shell fragments in high-energy marginal settings; (2) a change in the microstructure is not always visible due to the lack of structural changes in the growth lamellae (shell A); and (3) the cyclic repetition in the $\delta^{18}O$ pattern is considered the most reliable representation of an annual cycle, which is thereby defined as the interval between two $\delta^{18}O$ minima.

In shell A, five $\delta^{18}O$ cycles with 14 to 28 growth lamellae per year were identified resulting in an estimated growth rate of 6.1 to 10.7 mm/a. Shell B contains two complete $\delta^{18}O$ cycles with a lower number of growth lamellae per year (10 to 24) but an increased growth rate (7.2 to 13.7 mm/a). Two preserved

$\delta^{18}O$ cycles and corresponding growth lamellae (83 and 95) identified in shell D provide evidence for a much higher annual growth rate between 19.5 and 23.1 mm/a. The number of growth lamellae per year of shell A (14 to 28) and B (10 to 24) is comparable to the results of Regidor-Higuera *et al.* (2007), who counted 16 to 22 growth lamellae per year for a *Radiolites* sp. and 11 to 27 growth lamellae per year for a *Praeradiolites ciryi*. The vertical growth rate varies between 3.5–15 mm/a (Regidor-Higuera *et al.* 2007), which is in agreement with the range of shell A and B (6.1 to 13.7 mm/a). Shell D, in contrast, differs significantly with a growth rate of up to 26.4 mm/a, which is caused by the dominance of radial over vertical growth (Fig. 3). The slower growth rates of the RVs are caused by the predominance of vertical growth, which is favoured over radial growth (Fig. 3) in order to adapt to an unstable environment in a high-energy setting (Steuber 1996; Pons & Vicens 2008), in which the shells studied here lived.

Palaeoenvironmental implications

To reconstruct the prevailing environmental conditions of the rudists' living habitat, petrographic and elemental results were combined. First, the distribution of growth lamellae was used to reconstruct the living position of the bivalves within their marine habitat. In general, growth lamellae are divided into growth lines (dark) and growth increments (light). During emersion phases (low tides), when the shell is closed and the pH value decreases, dark lamellae are produced. During immersion (high tides), the shell opens and the pH value of the extrapallial fluid increases to values similar to the surrounding water (~ 7.8) and light lamellae are created (Regidor-Higuera *et al.* 2007). The durations of immersion and emersion phases are responsible for the width of one single lamellae. As the alternation of light and dark growth lamellae in the here analysed shells is often regular, a continuous change between immersion and emersion phases is assumed occurring in the intertidal domain. Such a habitat is in line with a high-energy setting located at the margin of a carbonate platform, which was reconstructed for the MLC section due to well-sorted and rounded shell debris.

Water temperatures from ancient waterbodies can be reconstructed using $\delta^{18}O$ as it is assumed that the organism produces its hard tissue in isotopic equilibrium with the surrounding water (Epstein *et al.* 1953) and the seawater $\delta^{18}O$ value is assumed to be –1 ‰VSMOW during the Cretaceous (e.g. Friedrich *et al.* 2012). However, some recent studies using clumped isotope thermometry have demonstrated that the assumption of a constant $\delta^{18}O_{H_2O(seawater)}$ value of –1 ‰VSMOW for deep time greenhouse settings may not be valid in all palaeoenvironments, and could be especially problematic in shallow marine successions (e.g. Jaffrès *et al.* 2007; Petersen *et al.* 2016; de Winter *et al.* 2021). Since the main purpose of this study is to investigate whether radiolitid shells represent suitable archives of Cretaceous seawater characteristics, the same parameters used in other studies, mainly Steuber (1999), were used here to allow for direct comparison.

For shell A, a range in sea surface temperature (SST) between 23°C and 30°C can be calculated. Shell B shows similar SST estimates with values between 24°C and 29°C. For shell C, only the LV, i.e., C1, was used for an SST estimate, as the few measured values of C2 do not show any cyclicity. The SSTs calculated for shell C1 show a very low variation, i.e., in the range of 27°C to 28°C. Shell D, considered as being exceptionally well preserved based on petrographic and elemental results, shows SST variations between 22°C and 29°C. All values and calculated temperatures are summarized in Table 1.

According to Steuber *et al.* (2005) mean temperatures derived from rudist skeletal carbonates from a similar setting and palaeolatitude do not exceed 32°C with most of their calculated values oscillating in a 20 to 25 °C range for the northern Tethys in the Early Cretaceous. Similar SSTs are obtained from foraminifera and TEX_{86} are in line with the radiolitid shells studied here (Fig. 16). Uncertainties of SST estimates are primarily associated with the uncertainty regarding the $\delta^{18}O$ value of ancient seawater (Steuber *et al.* 2005).

Conclusions

In this study, a first approach was made to combine petrographic and elemental results to determine whether radiolitid shells could represent a valuable archive for palaeoenvironmental reconstructions. In previous studies, radiolitids were rarely used for climate reconstruction due to their porous outer shell structure, as the diagenetic calcite filling the pores might compromise data collection. The following conclusions can be formulated based on the data obtained in this study:

1. Neither the isotopic nor the elemental datasets indicate a strong diagenetic alteration of shells A, B, C1 and D having either a non-compact or a compact shell structure. Only C2, which contains a cement-filled celluloprismatic structure, shows

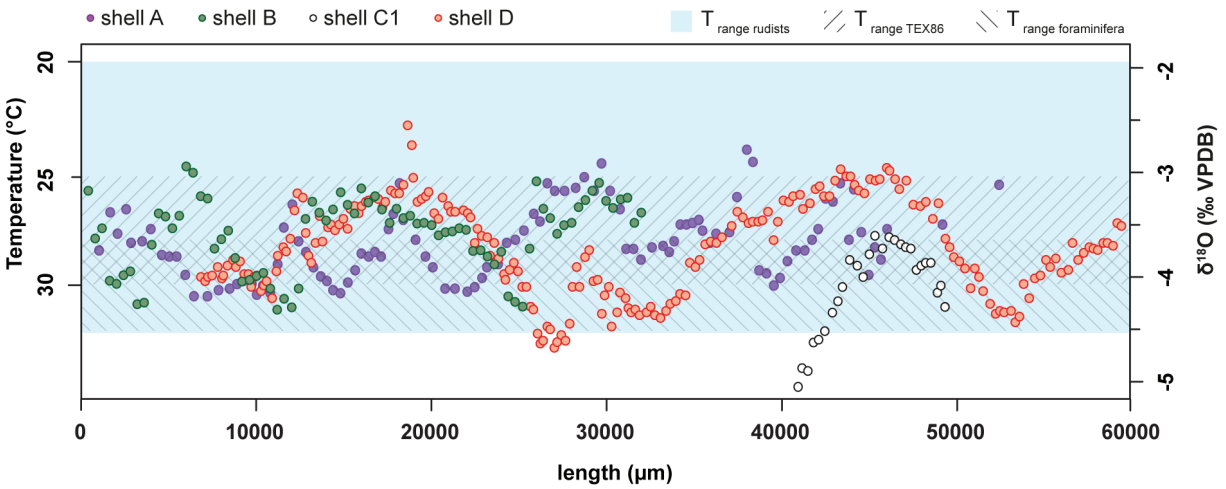

Fig. 16. The $\delta^{18}O$ values and calculated SSTs of shells A (RV; purple), B (RV; green), C1 (LV; white), D (LV; red) are plotted against the length (µm) and compared to value from radiolitids analysed by Steuber et al. (2005), TEX_{86} temperature data from the Aptian-Albian after O'Brien *et al.* (2017) and foraminifera data after Bottini *et al.* (2015).

highly variable isotopic and elemental data and is therefore classified as diagenetically altered.

2. The RV (shells A and B), which contains an alternation of compact and non-compact parts, often shows a $\delta^{18}O$ cyclic pattern.
3. The highly compact LV (shells C1 and D) records a gradually, smooth sinusoidal $\delta^{18}O$ pattern and is therefore a promising archive for palaeotemperature reconstruction.
4. Only RV (C2) of radiolitids, which is the only valve consisting exclusively of a cellulopristmatic structure, must be excluded for environmental reconstructions due to its high variability in both isotopes and elemental data.
5. Due to regular alternation of the growth lamellae, the intertidal zone is assumed to be the living habitat of the shell producing organism. The average growth rates for the right valve are 7.5 mm/a for shell A and 6.9 mm/a for shell B. The left valve (shell D) has a much faster growth rate of 14.9 mm/a.

In summary, a multi-proxy analysis of mid-Cretaceous radiolitid shells shows that it is possible to use them as a palaeoenvironmental archive. However, before radiolitids can be used as such, a petrographic (CL and µXRF mapping) screening and elemental (IRMS and µXRF line scans) analysis is highly recommended not only to rule out diagenetic alteration, but also to identify the shell structure. The latter determines whether climate reconstruction can be performed (only with compact and non-compact structure) or whether only the reconstruction of the habitat is possible (cellulopristmatic structure).

Acknowledgements. – We thank Christiane Wenske (LUH) for laboratory assistance. Financial support from German Research Foundation (DFG) project HU 2258/2-1 and HE 4467/8-1 is gratefully acknowledged. During this study, NdW was financed by a personal PhD fellowship from IWT Flanders (IWT700; now part of the Flemish Research Council, FWO). PC thanks the VUB strategic research fund and Research Foundation Flanders (FWO) for instrument funding.

References

Al-Aasm, I.S. & Veizer, J. 1986 a: Diagenetic stabilization of aragonite and low-Mg calcite; I, Trace elements in rudists. *Journal of Sedimentary Research 56*, 138–152. https://doi.org/10.1306/212f88a5-2b24-11d7-8648000102c1865d

Al-Aasm, I.S. & Veizer, J. 1986 b: Diagenetic stabilization of aragonite and low-Mg calcite; II, Stable isotopes in rudists. *Journal of Sedimentary Research 56*, 763–770. https://doi.org/10.2110/jsr.56.763

Anderson, T.F. & Arthur, M.A. 1983: Stable isotopes of oxygen and carbon and their application to sedimentologic and paleoenvironmental problems. In *Stable Isotopes in Sedimentary Geology*, ed. M. A. Arthur, T. F. Anderson, I. R. Kaplan, J. Veizer, L. S. Land, 1:1–151. Dallas: Soc. Econ. Paleontol. Mineral. https://doi.org/10.2110/scn.83.01.0000

Arthur, M.A., Williams, D.F. & Jones, D.S. 1983: Seasonal temperature-salinity changes and thermocline development in the mid-Atlantic Bight as recorded by the isotopic composition of bivalves. *Geology 11*, 655–659. https://doi.org/10.1130/0091-7613(1983)11<655:stcatd>2.0.co;2

Bodin, S., Meissner, P., Janssen, N.M., Steuber, T. & Mutterlose, J. 2015: Large igneous provinces and organic carbon burial: Controls on global temperature and continental weathering during the Early Cretaceous. *Global and Planetary Change 133*, 238–253. https://doi.org/10.1016/j.gloplacha.2015.09.001

Bornemann, A., Norris, R.D., Friedrich, O., Beckmann, B., Schouten, S., Sinninghe Damsté, J.S., Vogel, J., Hofmann, P. & Wagner, T. 2008: Isotopic evidence for glaciation during the Cretaceous supergreenhouse. *Science 319*, 189–192. https://doi.org/10.1126/science.1148777

Bottini, C., Erba, E., Tiraboschi, D., Jenkyns, H.C., Schouten, S. & Sinninghe Damsté, J.S. 2015: Climate variability and ocean fertility during the Aptian Stage. *Climate of the Past 11*, 383–402. https://doi.org/10.5194/cp-11-383-2015

Carpenter, S.J. & Lohmann, K.C. 1992: Sr/Mg ratios of modern marine calcite: Empirical indicators of ocean chemistry and precipitation rate. *Geochimica et Cosmochimica Acta 56*, 1837–1849. https://doi.org/10.1016/0016-7037(92)90314-9

Cestari, R. 1992: Biometrical analysis on Gorjanovicias and on other radiolitids (Radiolitidae, Hippuritoida). *Geologica Romana 28*, 1–25.

de Winter, N.J. & Claeys, P. 2016: Micro X-ray fluorescence (μXRF) line scanning on Cretaceous rudist bivalves: A new method for reproducible trace element profiles in bivalve calcite. *Sedimentology 64*, 231–251. https://doi.org/10.1111/sed.12299

de Winter, N.J., Goderis, S., Dehairs, F., Jagt, J.W.M., Fraaije, R.H.B., Van Malderen, S.J.M., Vanhaecke, F. & Claeys, P. 2017a: Tropical seasonality in the late Campanian (late Cretaceous): Comparison between multiproxy records from three bivalve taxa from Oman. *Palaeogeography, Palaeoclimatology, Palaeoecology 485*, 740–760. https://doi.org/10.1016/j.palaeo.2017.07.031

de Winter, N.J., Sinnesael, M., Makarona, C., Vansteenberge, S. & Claeys, P. 2017b: Trace element analyses of carbonates using portable and micro-X-ray fluorescence: performance and optimization of measurement parameters and strategies. *Journal of Analytical Atomic Spectrometry 32*, 1211–1223. https://doi.org/10.1039/c6ja00361c

de Winter, N.J., Müller, I.A., Kocken, I.J., Thibault, N., Ullmann, C.V. & Farnsworth, A. 2021: Absolute seasonal temperature estimates from clumped isotopes in bivalve shells suggest warm and variable greenhouse climate. *Communications Earth & Environment 2*, 1–8. https://doi.org/10.1038/s43247-021-00193-9

de Winter, N.J., Goderis S., Malderen, S.J.M.V., Sinnesael, M., Vansteenberge, S., Snoeck, C., Belza, J., Vanhaecke, F. & Claeys P. 2020: Subdaily-Scale Chemical Variability in a *Torreites Sanchezi* Rudist Shell: Implications for Rudist Paleobiology and the Cretaceous Day-Night Cycle. *Paleoceanography and Paleoclimatology 35*, e2019PA003723. https://doi.org/10.1029/2019pa003723

Eggins, S. & De Deckker, P., Marshall, J. 2003: Mg/Ca variation in planktonic foraminifera tests: implications for reconstructing palaeo-seawater temperature and habitat migration. *Earth and Planetary Science Letters 212*, 291–306. https://doi.org/10.1016/s0012-821x(03)00283-8

Elderfield, H. & Ganssen, G. 2000: Past temperature and δ18O of surface ocean waters inferred from foraminiferal Mg/Ca ratios. *Nature 405*, 442–445. https://doi.org/10.1038/35013033

Epstein, S., Buchsbaum, R., Lowenstam, H.A. & Urey, H.C. 1953: Revised carbonate-water isotopic temperature scale. *Geological Society of America Bulletin 64*, 1315–1325. https://doi.org/10.1130/0016-7606(1953)64[1315:rcits]2.0.co;2

Fenerci-Masse, M., Masse, J.P., Arias, C. & Vilas, L. 2006: *Archaeoradiolites*, a new genus from the Upper Aptian of the Mediterranean region and the origin of the rudist family Radiolitidae. *Palaeontology 49*, 769–794. https://doi.org/10.1111/j.1475-4983.2006.00573.x

Freitas, P.S., Clarke L.J., Kennedy, H., Richardson, C.A. & Abrantes, F. 2006: Environmental and biological controls on elemental (Mg/Ca, Sr/Ca and Mn/Ca) ratios in shells of the king scallop Pecten maximus. *Geochimica et Cosmochimica Acta 70*, 5119–5133. https://doi.org/10.1016/j.gca.2006.07.029

Friedrich, O., Norris, R.D. & Erbacher, J. 2012: Evolution of middle to Late Cretaceous oceans - a 55 my record of Earth's temperature and carbon cycle. *Geology 40*, 107–110. https://doi.org/10.1130/g32701.1

Frijia, G. & Parente, M. 2008: Strontium isotope stratigraphy in the upper Cenomanian shallow-water carbonates of the southern Apennines: Short-term perturbations of marine 87Sr/86Sr during the oceanic anoxic event 2. *Palaeogeography, Palaeoclimatology, Palaeoecology 261*, 15–29. https://doi.org/10.1016/j.palaeo.2008.01.003

Frijia, G., Parente, M., Di Lucia, M. & Mutti M. 2015: Carbon and strontium isotope stratigraphy of the Upper Cretaceous (Cenomanian-Campanian) shallow-water carbonates of southern Italy: Chronostratigraphic calibration of larger foraminifera biostratigraphy. *Cretaceous Research 53*, 110–139. https://doi.org/10.1016/j.cretres.2014.11.002

Hamama, H. 2010: Morphology and wall structure of some Turonian rudists (bivalvia, Hippuritoida) of Gabal Yelleg, northern Sinai, Egypt. *Journal of American Science 6*, 1682–1701.

Huck S. & Heimhofer, U. 2015: Improving shallow-water carbonate chemostratigraphy by means of rudist bivalve sclerochemistry. *Geochemistry, Geophysics, Geosystems 16*, 3111–3128. https://doi.org/10.1002/2015gc005988

Huck, S. & Heimhofer, U. 2021: Early Cretaceous Sea surface temperature evolution in subtropical shallow seas. *Scientific reports 11*, 1–9. https://doi.org/10.1038/s41598-021-99094-2

Huyghe, D., de Rafelis, M., Ropert, M., Mouchi,V., Emmanuel, L., Renard M. & Lartaud F. 2019: New insights into oyster high-resolution hinge growth patterns. *Marine Biology 166*, 48. https://doi.org/10.1007/s00227-019-3496-2

Jaffrés, J.B.D., Shields, G.A. & Wallmann, K. 2007: The oxygen isotope evolution of seawater: A critical review of a long-standing controversy and an improved geological water cycle model for the past 3.4 billion years. *Earth-Science Reviews 83*, 83–122. https://doi.org/10.1016/j.earscirev.2007.04.002

Kennedy, W.J. & Taylor, J.D. 1968: Aragonite in rudists. *Proceedings of the Geological Society of London 1645*, 325–331.

Klein, R.T., Lohmann, K.C. & Thayer, C.W. 1996: Sr/Ca and 13C/12C ratios in skeletal calcite of Mytilus trossulus: Covariation with metabolic rate, salinity, and carbon isotopic composition of seawater. *Geochimica et Cosmochimica Acta 60*, 4207–4221. https://doi.org/10.1016/s0016-7037(96)00232-3

Klein, R.T., Lohmann, K.C. & Thayer, C.W. 1996: Bivalve skeletons record sea-surface temperature and δ18O via Mg/Ca and 18O/16O ratios. *Geology 24*, 415–418. https://doi.org/10.1130/0091-7613(1996)024<0415:bsrsst>2.3.co;2

Mansour, A.S.M. 2004: Diagenesis of Upper Cretaceous rudist bivalves, Abu Roash area, Egypt: a petrographic study. *Geologia Croatica 57*, 55–66. https://doi.org/10.4154/gc.2004.03

Masse, J.P., Fenerci-Masse, M., Vilas, L. & Arias, C. 2007: Late Aptian-Albian primitive Radiolitidae (bivalves, hippuritoidea) from Spain and SW France. *Cretaceous Research 28*, 697–718. https://doi.org/10.1016/j.cretres.2006.09.004

Masse, J.P. & Maresca, M.G. 1997: Late Aptian Radiolitidae (rudist bivalves) from the Mediterranean and Southwest Asiatic regions: taxonomic, biostratigraphic and palaeobiogeographic aspects. *Palaeogeography, Palaeoclimatology, Palaeoecology 128*, 101–110. https://doi.org/10.1016/s0031-0182(96)00049-1

Marali, S., Schöne, B.R., Mertz-Kraus, R., Griffin, S.M., Wanamaker, A.D., Butler, P.G., Holland, H.A. & Jochum, K.P. 2017: Reproducibility of trace element time-series (Na/Ca, Mg/Ca, Mn/Ca, Sr/Ca, and Ba/Ca) within and between specimens of the bivalve Arctica islandica – A LA-ICP-MS line scan study. *Palaeogeography, Palaeoclimatology, Palaeoecology 484*, 109–128. https://doi.org/10.1016/j.palaeo.2016.11.024

Mutterlose, J., Bornemann, A. & Herrle, J. 2009: The Aptian–Albian cold snap: Evidence for 'mid' Cretaceous icehouse interludes. *Neues Jahrbuch für Geologie und Paläontologie-Abhandlungen 252*, 217–225. https://doi.org/10.1127/0077-7749/2009/0252-0217

O'Brien, C.L., Robinson, S.A., Pancost, R.D., Damsté, J.S.S., Schouten, S., Lunt, D.J., Alsenz, H., Bornemann, A., Bottini, C., Brassell, S.C., Farnsworth, A., Forster, A., Huber, B.T., Inglis, G.N., Jenkyns, H.C., Linnert, C., Littler, K., Markwick, P., McAnena, A., Mutterlose, J., Naafs, B.D., A., Püttmann, W., Sluijs, A., Helmond, N.A.G.M. van, Vellekoop, J., Wagner, T. & Wrobel, N.E. 2017: Cretaceous sea-surface temperature evolution: Constraints from TEX86 and planktonic foraminiferal oxygen isotopes. *Earth-science reviews 172*, 224–247. https://doi.org/10.1016/j.earscirev.2017.07.012

Pejović, D. 1994: New rudist species from Lesak area in theIbar valley (Vardar zone). *Vesnik Geologija*, 45–61.

Petersen, S.V., Tabor, C.R., Lohmann, K.C., Poulsen, C.J., Meyer, K.W. & Carpenter, S.J. 2016: Temperature and salinity of the Late Cretaceous western interior seaway. *Geology 44*, 903–906. https://doi.org/10.1130/g38311.1

Pons, J.M. & Vicens, E. 2008: The structure of the outer shell layer in radiolitid rudists, a morphoconstructional approach. *Lethaia 41*, 219–234. https://doi.org/10.1111/j.1502-3931.2007.00048.x

Poulsen, C.J., Barron, E.J., Peterson, W.H. & Wilson, P.A. 1999: A reinterpretation of mid-Cretaceous shallow marine temperatures through model-data comparison. *Paleoceanography 14*, 679–697. https://doi.org/10.1029/1999pa900034

Regidor-Higuera, I., García-Garmilla, F. & Skelton, P.W. 2007: Sclerochronology and diagenesis of Late Cretaceous radiolitids (Bivalvia, Hippuritoidea), Spain. *In:* Scott, R.W. (Ed.), *Cretaceous Rudists and Carbonate Platforms: Environmental Feedback. SEPM Special Publication 87*, 115–140. https://doi.org/10.2110/pec.07.87.0115

Rosenberg, G.D. & Hughes, W.W. 1991: A metabolic model for the determination of shell composition in the bivalve mollusc, *Mytilus edulis*. *Lethaia 24*, 83–96. https://doi.org/10.1111/j.1502-3931.1991.tb01182.x

Ross, D.J. & Skelton, P.W. 1993: Rudist formations of the Cretaceous: a palaeoecological, sedimentological and stratigraphical review. *Sedimentology Review 1*, 73–91. https://doi.org/10.1002/9781444304534.ch5

Rush, P.F. & Chafetz, H.S. 1990: Fabric-retentive, non-luminescent brachiopods as indicators of original $\delta^{13}C$ and $\delta^{18}O$ composition; a test. *Journal of Sedimentary Research 60*, 968–981. https://doi.org/10.1306/d4267659-2b26-11d7-8648000102c1865d

Sanders, D. 1999: Shell disintegration and taphonomic loss in rudist biostromes. *Lethaia 32*, 101–112. https://doi.org/10.1111/j.1502-3931.1999.tb00528.x

Schmitt, K., Heimhofer., Frijia. G., di Lucia, M. & Huck, S. 2019: Deciphering the fragmentary nature of Cretaceous shallow water limestone archives: A case study from the subtropical Apennine carbonate platform. *Newsletters on Stratigraphy 53*, 389–413. https://doi.org/10.1127/nos/2019/0551

Schöne, B. R., Zhang, Z., Radermacher, P., Thébault, J., Jacob, D.E., Nunn, E.V. & Maurer A.-F. 2011: Sr/Ca and Mg/Ca ratios of ontogenetically old, long-lived bivalve shells (Arctica islandica) and their function as paleotemperature proxies. *Palaeogeography, Palaeoclimatology, Palaeoecology 302*, 52–64. https://doi.org/10.1016/j.palaeo.2010.03.016

Schumann, D. 1995: Upper cretaceous rudist and stromatoporid associations of Central Oman (Arabian Peninsula). *Facies 32*, 189–202. https://doi.org/10.1007/bf02536868

Schumann, D. & Steuber, T. 1997: Rudisten. Erfolgreiche Siedler und Riffbauer der Kreidezeit. *Städte unter Wasser-2 Milliarden Jahre.-Kleine Senckenberg-Reihe 24,* 117–122.

Scott, R.W. 1995: Global environmental controls on Cretaceous reefal ecosystems. *Palaeogeography, Palaeoclimatology, Palaeoecology 119*, 187–199. https://doi.org/10.1016/0031-0182(94)00068-9

Shackleton, N.J. & Kennett, J.P. 1975: Paleotemperature history of the Cenozoic and the initiation of Antarctic glaciation: Oxygen and carbon isotope analyses in DSDP sites 277, 279, and 281. *In Initial reports of the Deep Sea Drilling Project, Volume 29*: Washington, D. C., U.S. Government Printing Office, 743–755. https://doi.org/10.2973/dsdp.proc.29.117.1975

Skelton, P.W. 1974: Aragonitic shell structures in the rudist *Biradiolites*, and some palaeobiological inferences. *Géologie méditerranéenne 1*, 63–74. https://doi.org/10.3406/geolm.1974.928

Skelton, P.W. 1978: The evolution of functional design in rudists (Hippuritacea) and its taxonomic implications. *Philosophical Transactions of the Royal Sociery London, B 284*, 305–318. https://doi.org/10.1098/rstb.1978.0069

Skelton, P.W. 2003: Changing Climate and biota in the marine record. In: Skelton, P.W. (Ed.), *The Cretaceous World.* Cambridge University Press, Cambridge, 163–184. https://doi.org/10.1086/425766

Skelton, P.W. & Gili, E. 1991: Palaeoecological classification of rudist morphotypes. In *First International Conference on Rudists, Proccedings, Serbian Geological Society, Belgrade,* 71–86.

Skelton, P.W. & Gili, E. 2012: Rudists and carbonate platforms in the Aptian: a case study on biotic interactions with ocean chemistry and climate. *Sedimentology 59*, 81–117. https://doi.org/10.1111/j.1365-3091.2011.01292.x

Steuber, T. 1994: New rudist (Radiolitidae) from the Upper Cretaceous of Boeotia, Central Greece. *Paläontologische Zeitschrift 68*, 43–62. https://doi.org/10.1007/bf02989432

Steuber, T. 1996: Stable isotope sclerochronology of rudist bivalves: growth rates and Late Cretaceous seasonality. *Geology 24*, 315–318. https://doi.org/10.1130/0091-7613(1996)024<0315:sisorb>2.3.co;2

Steuber, T. & Löser, H. 2000: Species richness and abundance patterns of Tethyan Cretaceous rudist bivalves (Mollusca: Hippuritacea) in the central-eastern Mediterranean and Middle East, analysed from a palaeontological database. *Palaeogeography, Palaeoclimatology, Palaeoecology 162*, 75–104. https://doi.org/10.1016/s0031-0182(00)00106-1

Steuber, T. & Rauch, M. 2005: Evolution of the Mg/Ca ratio of Cretaceous seawater: implications from the composition of biological low-Mg calcite. *Marine Geology 217*, 199–213. https://doi.org/10.1016/j.margeo.2005.02.012

Steuber, T., Rauch, M., Masse, J.P., Graaf, J. & Malkoč, M. 2005: Low-latitude seasonality of Cretaceous temperatures in warm and cold episodes. *Nature 437*, 1341. https://doi.org/10.1038/nature04096

Steuber, T. & Schlüter, M. 2012: Strontium-isotope stratigraphy of Upper Cretaceous rudist bivalves: biozones, evolutionary patterns and sea-level change calibrated to numerical ages. *Earth-Science Reviews 114*, 42–60. https://doi.org/10.1016/j.earscirev.2012.04.004

Steuber, T. & Veizer, J. 2002: Phanerozoic record of plate tectonic control of seawater chemistry and carbonate sedimentation. *Geology 30*, 1123–1126. https://doi.org/10.1130/0091-7613(2002)030<1123:proptc>2.0.co;2

Steuber. T. 1999: Isotopic and chemical intra-shell variations in low-Mg calcite of rudist bivalves (Mollusca-Hippuritacea): disequilibrium fractionations and late Cretaceous seasonality. *Int. Journ. Earth Sciences 88*, 551–570. https://doi.org/10.1007/s005310050284

Tibljaš, D., Moro, A. & Ostrež, Ž. 2004: Mineral and chemical composition of rudist valves from Upper Cretaceous limestones of Southern Istria, Croatia. *Geologia Croatica 57*, 73–79. https://doi.org/10.4154/gc.2004.05

Watanabe, T., Winter, A. & Oba, T. 2001: Seasonal changes in sea surface temperature and salinity during the Little Ice Age in the Caribbean Sea deduced from Mg/Ca and 18 O/16 O ratios in corals. *Marine Geology 173*, 21–35. https://doi.org/10.1016/s0025-3227(00)00166-3

Woo, K.S., Anderson, T.F. & Sandberg, P.A. 1993: Diagenesis of skeletal and nonskeletal components of mid-Cretaceous limestones. *Journal of Sedimentary Research 63*, 18–32. https://doi.org/10.1306/d4267a7d-2b26-11d7-8648000102c1865d

Yan, H., Liu, C., An, Z., Yang, W., Yang, Y., Huang, P., Qiu, S., Zhou, P., Zhao, N. & Fei H. 2020: Extreme weather events recorded by daily to hourly resolution biogeochemical proxies of marine giant clam shells. *Proceedings of the National Academy of Sciences 117*, 7038–7043. https://doi.org/10.1073/pnas.1916784117